NORTHWESTERN UNIVERSITY

Trapped Ion Thermometry and Mass Determination through Imaging

A DISSERTATION

SUBMITTED TO THE GRADUATE SCHOOL

IN PARTIAL FULFILLMENT OF THE REQUIREMENTS

for the degree

DOCTOR OF PHILOSOPHY

Field of Physics and Astronomy

By

Vaishnavi Rajagopal

EVANSTON, ILLINOIS

June 2014

ABSTRACT

Trapped Ion Thermometry and Mass Determination through Imaging

Vaishnavi Rajagopal

Recent advances in tunable lasers and ion-trap fabrication has led to the development of very precise state preparation and manipulation schemes for trapped atomic and molecular ions. Housed in an ultra high vacuum (UHV) chamber (with pressures in the $\sim 10^{-10}$ - 10^{-11} torr range), these ions are confined to an almost collision-free environment resulting in long lifetimes ($\sim$hours) important for many experiments ranging from fundamental physics, quantum computing, condensed matter simulations to cold chemistry. Though the actual trap and laser parameters for specific experiments vary, there are some common requirements. For instance, experiments on quantum computation require very small (3-4mm) and hence tightly bound traps with deep potential wells ($\sim$10eV), so that the ions are well into the quantum regime. Complementing this effort, there is also great interest in studying Coulomb crystals involving a large number of ions, which require larger ($>$10mm) and hence weakly bound traps with shallower potential wells (2-3eV). This is the regime explored in our work with the spin-zero ^{138}Ba$^+$ atomic ions. Standard laser-cooling techniques are applied to Doppler-cool the motional degrees of freedom of these trapped ions, allowing us to image individual ions and probe various characteristics in-situ.

This thesis begins with an Introduction to the ion-trap design we built for our experiments followed by an overview of the methods for trapping, cooling and imaging trapped ions. In Chapter 2, we report the first use of the measurement of the spatial profile of emitted fluorescence to determine the temperatures of individual laser-cooled ions in linear Coulomb crystals with high precision. Our technique employs the same imaging apparatus that is used for monitoring the ions and opens up possibilities for equilibrium temperature measurement of strings in the presence of dark ions. It can potentially be applied to monitor ion temperatures in-situ for the study of ion-neutral cold chemical reactions. Chapter 3 discusses a method to determine the chemical composition of sympathetically cooled molecular ions co-trapped with laser-cooled atomic ions in a two-species mixed string. Our technique uses the thermal spatial spread of laser-cooled atomic ions to measure the secular-resonance frequency of vibration of the mixed string, from which the mass of the molecular ion is inferred. Further, our apparatus for making molecular ions provides high local density that can potentially be used for studying cold chemical reactions with small cross-sections, in addition to a fast UHV recovery time ($\sim$1 second) to allow for fast measurements after the reactant gas is introduced. The last chapter includes preliminary calculations for proposed molecular candidates amenable to laser-cooling and recyclable spectroscopy. In particular, the 1+1'-Resonance-Enhanced Multi-Photon Dissociation (REMPD) schemes for characterizing the proposed molecular ions are discussed. Here, our choice of $^{138}\text{Ba}^+$ as the atomic ion is advantageous as it has one of the longest wavelength laser-cooling transitions. This implies that the laser-cooling photons have the least energy and one can investigate a larger class of molecules without accidentally dissociating them.

Acknowledgements

Every person's experience is unique and we learn how to be or not to be from the people around us. In that sense, I'm very thankful to everyone I met in my life. But the few people mentioned below, in the past five years, have directly influenced who I'm as a person and researcher in a way that I've noticed a difference. I'm truly grateful for their association with me.

"A person who never made a mistake never tried anything new, said Albert Einstein. But let us agree on a reasonable proportion of things working to not working," said Prof. Brian Odom when I joined the lab. Right from guiding me step by step in the first few years of graduate school, teaching me to be extra thorough with my ideas to letting me grow as a researcher, Brian has been a great adviser. It always felt better to see Brian in the lab when equipment broke or when I had no idea how to solve a problem. In addition to saying "I'm sure you will figure it out" he always gave good ideas that instantly made the situation look much better. Thanks for the five-odd wonderful years. Prof. Ketterson's questions on our experiments' place in the grander scheme of science have always opened up new angles of looking at my measurement that I had not previously thought about. Thanks for your guidance. Discussions with Prof. Jens Koch and his comments on my thesis have taught me to express my ideas better. I'm greatly thankful for your help and guidance. Thanks to Prof. Arthur Schmidt and Prof. Deborah Brown for teaching me to be a more

efficient TA. If it were not for their guidance, I would not have enjoyed interacting with 100+ students in class.

A very large part of graduate life is spent in the lab. It definitely would not have felt like second home if it weren't for the wonderful friends and colleagues I had in the Odom Group. As someone I closely worked with for a long time, Joan has definitely influenced my book keeping and organization skills. Thanks for all the help in setting up the experiment! Right from building the first trap, lifting heavy chambers for baking to all the machine shop advice, David and I have had some great times. Always ready to lend a hand or just hangout, Chien-yu has been a great buddy. I joke that his signature is present in all my experiments. Yen-Wei's expertise on equipment (and chocolate) have saved me hours that I would have otherwise spent reinventing the wheel (feeling unhappy). Being the only one who cleans my side of the table on cleaning turns, Chris has significantly improved my lab's living condition. Ming-Feng's dinner meet-ups and driving coaching never fails to cheer and amuse me. Working with fast-learner Mark K, discussing physics with Pat S and hanging out with Jason, Irina, Marc and Lauren have all been very enjoyable. I definitely developed a close bond when they made me balance water bottles on my head when passing my station, irritated me by playing songs on fishes, shared their apples/chocolate milk/peanuts and let me hold the record for highest sit-ups in the group Olympics for 2 months. Thank you! It has been a pleasure knowing you all. Special thanks to Joan, Jason, David, Chien-Yu and Scott for their help in the lab during the days I was recovering from sports injury. I could not have done it without your help!

Outside of work, I have enjoyed hysterical laughs in the middle of the night reading H2G2, girl talk, BYOL and crib sessions, making IGSSA videos at mid night, dance and music practices, Diwali puja, swimming, muholla-Sunday brunches, fancy home-cooked

that I had made one for life. For if I had known, I would have never waited this long to get to know you. I intend to prove Socrates wrong by helping you to continue philosophizing while staying happy. I look forward to all that life has to offer with you!

It is indeed easier to learn flying when you know that you'll hit a trampoline when you fall. With their kindness and all embracing lifestyle, my parents Smt. K. Meenakshi and Dr. A. Rajagopal have been great role-models and best friends. They have nursed me back physically and emotionally every single time I was hurt and put me back on track to face my life. Amma and Appa, I truly feel lucky to be your daughter. Your strength and unconditional love will always keep me strong and happy.

I would like to thank God for giving me the interest and opportunity to wonder deeply about this fascinating world.

P.S: Thanks to Brian, Vivek, Joan and David for proof-reading all my work.

Dedication

To my parents.

Table of Contents

CHAPTER 1

Basics of Ion-Trapping

1.1. Introduction

Charged particles cannot be trapped in a configuration of static electric potentials $U(\mathbf{R})$, since Gauss's law $\nabla^2 U(\mathbf{R}) = 0$ allows only saddle points and no minima solutions [1]. Also known as Earnshaw's theorem, this condition is no longer a constraint in Penning and Paul traps which use cyclotron motion of the ion in a plane and high frequency oscillation of the potential around an ion's saddle point, respectively, to hold ions for longer periods of time. These two traps cater to different types of experiments depending on magnetic field requirements. In this chapter, details of a linear Paul trap that we built for our experiments (Fig. 1.1), our experimental chamber assembly (Fig. 1.2) and other practical considerations for building apparatus will be discussed.
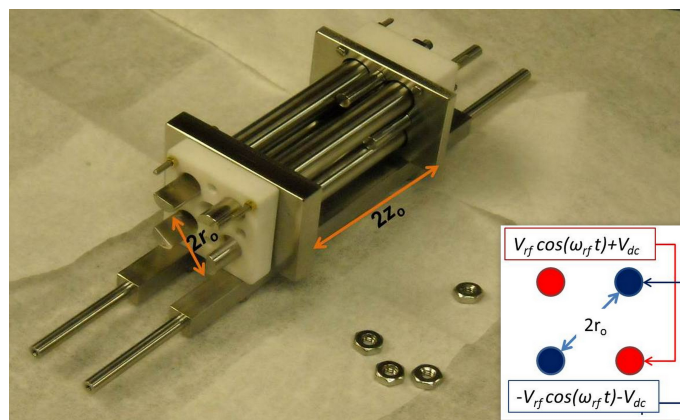
Figure 1.1. Picture of our assembled linear Paul trap. Ions are axially confined by a positive voltage applied to the endcaps (plates with short electrodes) that are $2z_o$ apart. Radial confinement is provided by the rf voltages applied to the four rod electrodes as shown in the inset.

Figure 1.2. Assembled trap housed inside an octagonal vacuum chamber.

1.2. Making Ions

An atomic beam of neutral barium is produced in the UHV chamber by heating elemental barium in an alumina tube (p/n: 713-654-51- Good fellow) using a thorinated tungsten wire wound around the tube as shown in Fig. 1.3. One end of the tube is sealed off using an oxy-acetylene torch and it is then packed with neutral barium in an inert nitrogen atmosphere. Two holes are drilled into the bottom of the tube to fit in a K-type thermocouple (Alumel and Chromel: p/n: SPCH-005-50, SPAL-005-50- Omega) for temperature measurement of the barium. The oven is filled with elemental barium in a nitrogen atmosphere. Typical temperatures of about 400- 450 °C are reached for loading ions in our trap. The oven is placed off-center from the trap in the slot shown in the CAD drawing of the mount in Fig. 1.4. This helps avoid coating barium on the electrodes close to the center and hence minimizes patch potentials. The three clearance holes, drilled on a 1" diameter circle, are used for mounting the oven off a base that forms an exit chamber, and the 0.125" hole at the center facilitates a pump out scheme described in Chapter 3.
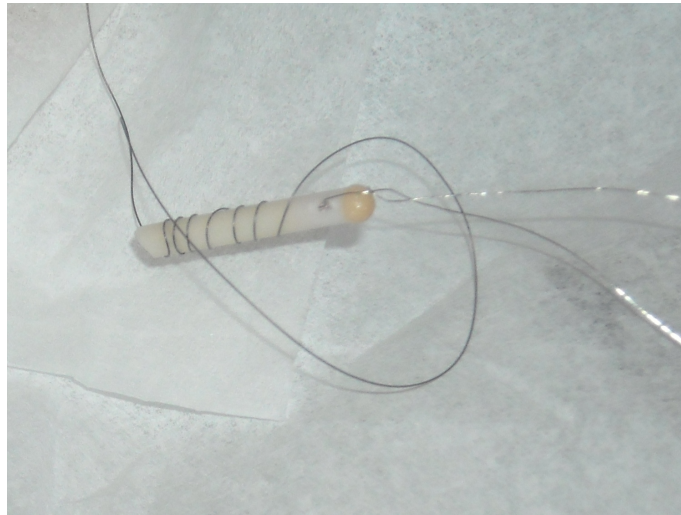
Figure 1.3. Picture of a tungsten wire wound around an alumina tube with a thermocouple attached at the sealed end.
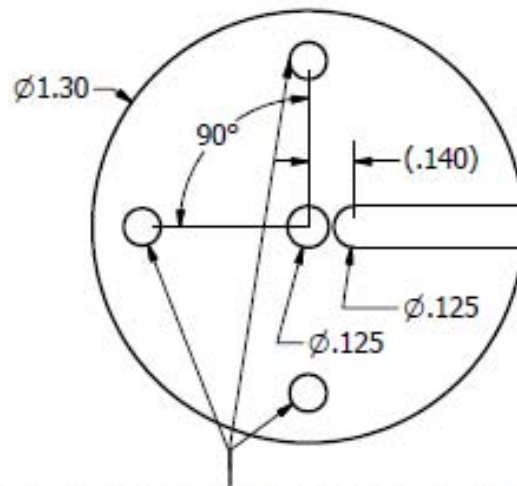
Three holes @ 90 degrees on a 1" diameter circle; Tight fit for 4-40 thread

Figure 1.4. Picture of the mount (made out of macor) used for mounting the oven off the center of the trap.

1.2.1. Two-photon Ionization

Ba^+ ions are loaded in the trap by using one of three possible two-photon ionizing schemes as summarized in Fig. 1.5(a) [2] [3] [4]. An ECDL (external cavity diode laser, Toptica-Pro) at 780nm (tuned to 791nm) with an output power of 8 mW, frequency-locked using a wavemeter (High finesse - p/n: WS-U) to within 2-3 MHz, excites the neutral barium beam from the $^1S_0$ to $^3P_1$ state. To load the ^{138}Ba isotope, this laser is red-detuned by 106 MHz from the 791nm transition. Our two-photon (791 nm + N_2 laser at 341nm and 791 nm + 310 nm) ionization procedures are similar to the prescription in references [2] [4]. Our third 1+1 photo ionization scheme using a 413nm laser is prescribed in Ref. [3]. The lasers corresponding to any one of these three schemes are carefully aligned to overlap with the neutral atom beam from the oven. On ionization, the ions experience the trap potential and remain trapped. We are able to load pure ^{138}Ba ions with our setup since the linewidth of the $^1S_0$ to $^3P_1$ transition is narrow ($\sim$50 kHz) and any Doppler broadening of this transition is insignificant as we are loading perpendicular to direction of the beam. Also, the frequencies for loading the other isotopes are well separated from that for loading ^{138}Ba [4] [5]. Naturally occurring barium has an abundance of 78% for ^{138}Ba giving us higher loading rates for this isotope.
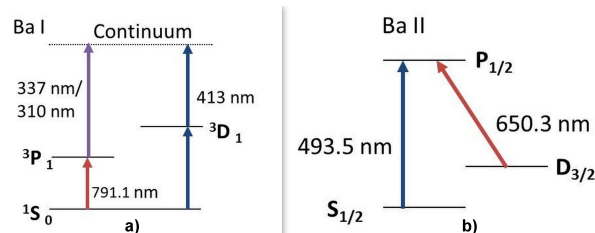
Figure 1.5.   Relevant energy level diagrams for (a) neutral ^{138}Ba, (b) $^{138}Ba^+$

1.3. Trapping Ions

A linear Paul trap consists of four rod electrodes with their centers placed symmetrically in a circle of radius a. Two sinusoidal voltages (V_{rf}), 180 degrees out of phase with respect to each other, are applied to two diagonally opposite pairs of electrodes as shown in Fig. 1.1. This configuration produces a pseudo-potential that traps the ions in the radial direction. DC voltages (V_{ec}) are applied to the two endcaps, in our case two plate electrodes with rods at a distance of $2z_o$ in order to confine the ions axially.

1.3.1. Radial and Axial Potentials

The quadrupole potential (U) for the configuration when $(V_{rf}\cos(\omega_{rf}t)+V_{dc})$ is applied to one pair of diagonally opposite rods and $-(V_{rf}\cos(\omega_{rf}t)+V_{dc})$ applied to the other pair of rods is given by Eq. 1.1. Though the next higher order in the multi-pole expansion of the potential (U) for this symmetry has c_6 terms [1], these are not significant close to the trap axis [6]. Here $2r_o$ is the distance between any two diagonal rods.

(1.1)
$$U = \frac{1}{2r_o^2}(x^2 - y^2)(V_{rf}\cos(\omega_{rf}t) + V_{dc})$$

Consider the force on the ions, as a function of displacement X_o, to have two components: one that is static $(F(X_o))$ and another $(f(X_o,t))$ generating high frequency oscillations at ω_{rf} around X_o. For time scales longer than $1/\omega_{rf}$ the particle oscillates in a smooth motion known as the secular motion with displacement given by X_o. f(X_o,t) causes high frequency micromotion S(X_o) around X_o at the carrier frequency ω_{rf} [7] [8] [9].

---

[1]To preserve the radial symmetry only even order terms c_{2n} (c_2, c_4, c_6..etc) are present in the multipole expansion of the potential for this configuration. Further, because of the quadrupole symmetry, only c_{4n+2} terms (c_2, c_6, c_{10}..etc) make non-zero contribution to the potential.

For the approximation $X_o \gg S$ and $\ddot{X}_o \ll \ddot{S}$, it can be shown that the force equations reduce to Eq. 1.2 [10].

$$(1.2) \quad m(\ddot{X}_o + \ddot{S}) = F(X_o) + f(X_o, t) + S\left(\left.\frac{\delta F}{\delta x}\right|_{x=X_o} + \left.\frac{\delta f(x, t)}{\delta x}\right|_{x=X_o}\right) + O(S^2)...$$

Equating the fast oscillating terms on either side of Eq. 1.2, the micromotion amplitude can be shown to oscillate at the same frequency as the driving force but with a phase difference of π.

$$(1.3) \qquad m\ddot{S} \approx f(X_o, t)$$

$$(1.4) \qquad S(X_o, t) \approx \frac{1}{m\omega_{rf}^2} f_o(X_o) \cos(\omega_{rf}(t - t_o) + \pi)$$

Averaging over a period of the micromotion, using the amplitude of micromotion given above, we get

$$(1.5) \qquad m\ddot{X}_o = F(X_o) - \frac{1}{m\omega_{rf}^2} \frac{1}{\tau_{rf}} \int_0^{\tau_{rf}} f_o(X_o) \frac{\partial f(x, t)}{\partial x} \, \mathrm{d}x.$$

$$(1.6) \qquad m\ddot{X}_o = F(X_o) - \frac{1}{m\omega_{rf}^2} f_o(x) \left.\frac{\partial f_o(x)}{\partial x}\right|_{x=X_o}$$

Rewriting the force equation in terms of potentials with static $U_F(x)$ and oscillating components $\phi_{ps}(x)$, we get

$$(1.7) \qquad m\ddot{X}_o = -\frac{\partial}{\partial x}(\phi_{sec}(x)) = -\frac{\partial}{\partial x}(QU_F(x) + \phi_{ps}(x))$$

with the pseudo potential given by

$$(1.8) \qquad \phi_{ps} = \frac{Q^2}{mw_{rf}^2}\left(\frac{Vrf}{2r_o^2}\right)(x^2 + y^2)$$

A DC voltage applied to the endcaps has a potential satisfying $\nabla^2(\text{U}) = 0$ given by Eq. 1.9. The applied potential is scaled by a dimensionless geometric factor κ that depends on the geometry of the endcap electrodes. To determine this factor, we simulated $U_{ec}(x, y, z)$ for our trap with the program Simion [11] and verified it to within 2% by measuring the axial secular frequency as a function of the endcap voltage V_{ec}. z_o in Eq. 1.9 is half the distance between the endcaps.

$$(1.9) \qquad U_{ec}(x, y, z) = \frac{\kappa V_{ec}}{z_o^2}\left(z^2 - \frac{1}{2}(x^2 + y^2)\right)$$

1.3.2. Rotated Endcap Trap (RET) design

The trap electrodes made out of SS 304 are mounted off of two macor plates which electrically isolate the different electrodes (see Fig. 1.1). The electrodes are electro-polished to ensure smooth electrical surfaces. The macor plates are then mounted on two platform rods that are held by two groove grabbers on either side of an octogon's (MCF600-SphOct-F2C8) diagonally opposite 2.75" ports (see Fig. 1.2). Electrical connection is made by connecting a wire spot-welded to the electrodes through a UHV compatible feed-through. A quadrupole power supply (Ardara) with computer controlled offsets or a home-built toroidal resonator with an amplifier is used to provide rf voltage to the rod electrodes.

List of trap parameters

Frequency of the rf power supply ω_{rf}= 2.85 MHz

Radius of the circle a= 8.6mm.

Distance between the endcaps $2z_o$= 17.78mm.

Diameter of the rod electrode $2R_e$= 8mm .

Diameter of the endcap electrode $2R_{ec}$= 4mm.

Diameter of the center hole of the macor for laser axis: 7.6 mm.

Length of each of the endcap electrode: 6.45 mm.

Distance between the diagonally opposite electrodes $2r_o$= 9.2 mm.

Geometric factor for the endcaps $\kappa = 0.059$.

Further away from the axis, c_6 terms become significant in our trap since the ratio of $R_e/(r_o)$ is not equal to 1.148 [**6**].
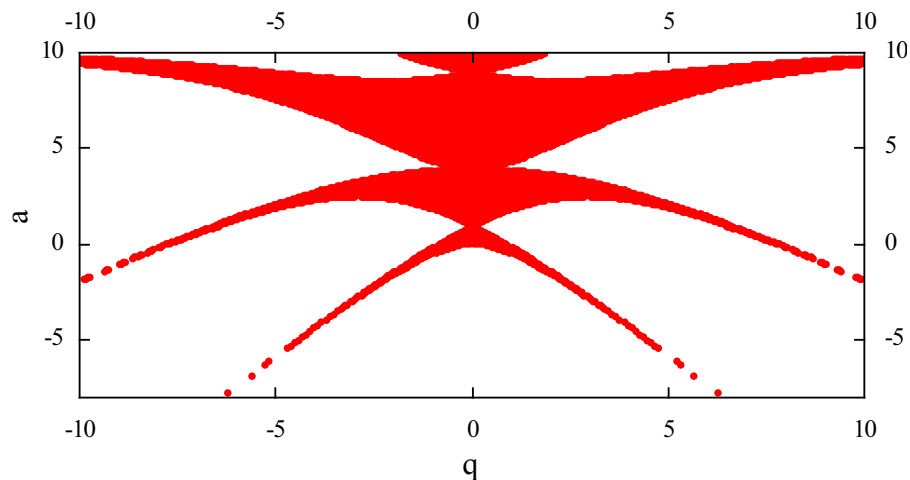
Figure 1.6.   Stability diagram for ions in the dimensionless a-q space along the x axis.

1.3.3. Motion of a charged particle in the trap

The effective potential experienced by ions of charge Q in the trap is given by the combined potential in Eq. 1.1 and Eq. 1.9. Rewriting the corresponding force equation in a parametric form, we get Eq. 1.10, generally known as the Mathieu equation. Floquet's theorem offers a general solution to Mathieu's equation [12] and the stable solutions can be obtained using standard numerical (eg. Mathematica) codes.

$$(1.10) \qquad \frac{d^2 X_j}{d\tau} = (a_j - 2q_j \cos(2\tau))X_j = 0$$

where the parameters τ, a and q are given below.

$$(1.11) \qquad \tau \;=\; \frac{1}{2}\omega_{rf}t$$

$$(1.12) \qquad a_x \;=\; \frac{4Q}{m\omega_{rf}^2}\left(-\frac{\kappa V_{ec}}{z_o^2} + \frac{U_{dc}}{r_o^2}\right)$$

$$(1.13) \qquad a_y \;=\; -\frac{4Q}{m\omega_{rf}^2}\left(\frac{\kappa V_{ec}}{z_o^2} + \frac{U_{dc}}{r_o^2}\right)$$

$$(1.14) \qquad a_z \;=\; -\frac{4Q}{m\omega_{rf}^2}\left(\frac{2\kappa V_{ec}}{z_o^2}\right)$$

$$(1.15) \qquad q_x \;=\; -q_y = \frac{2V_{rf}}{m\omega_{rf}^2 r_o^2}$$

$$(1.16) \qquad q_z \;=\; 0$$

The stable regions in the (a, q) space are plotted in Fig. 1.6. The complete solution for equations in both X and Y are obtained by super-imposing the solutions for each equation [13]. In our trap, the region of interest is close to the origin with typical $a_x \approx 3 \times 10^{-1} \; V_{dc}/m(amu)$, $q_x \approx 2.57 \times 10^{-2} V_{rf}/m(amu)$ and $a_z \approx 2 \times 10^{-4} V_{ec}/m(amu)$. The

appropriate a and q translated in the V_{rf} and V_{dc} parameters for a $V_{ec} = 30$ V is given in Fig. 1.7. This stability diagram shows that at low V_{rf} (around 300 Vpp) and low V_{dc} on the rf rods (around 3 volts), we can make the trap stable for lighter masses and unstable for heavier masses. We use this technique to eject any heavier molecule formed in our trap as illustrated in Fig. 1.8.
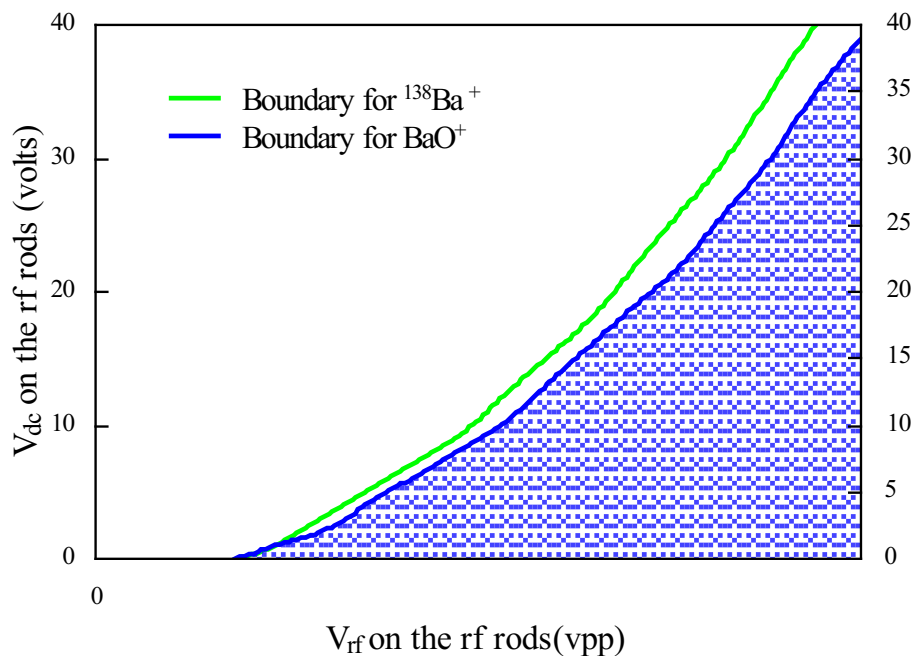
Figure 1.7. Stability diagram in terms of our trap parameters for ^{138}Ba$^+$ and BaO$^+$. The blue shaded region in the plot is stable for both ^{138}Ba$^+$ and BaO$^+$ where as the region between the blue and green curves is stable only for ^{138}Ba$^+$. Both the species are unstable left of the green curve.

1.3.4. Vaccum chamber

The trap is housed in a UHV chamber which is brought down to a pressure of 1×10^{-10} torr using an ion pump (Gamma Vacuum: p/n PN 900013), a getter pump (Saes: p/n D400-2) and a turbo pump (Edwards: EXT76DX) with roughing pump (Edwards: XDS-5). A Pneumatic valve (Edwards: p/n LCPV25EKA) is attached between the turbo and
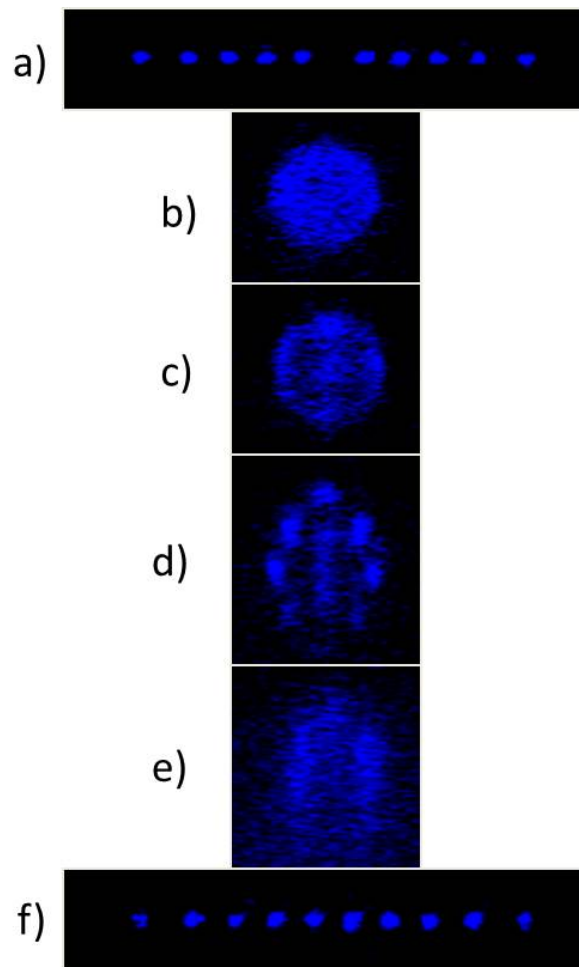
Figure 1.8. (a) through (f) is a typical sequence of fluorescence images of ions as a dark ion is dumped from the trap. (a) contains 10 bright ions and one molecular ion in a linear string. The lack of fluorescence in one site is an indication of non-fluorescing species. At higher V_{ec} ((b) through (e)), ions form a 3-d shape. V_{dc} is varied from (b) through (e), until the non-fluorescing ion becomes unstable and leaves the trap in (e). (f) shows the 10 bright ions resulting from our technique.

the roughing pump to protect UHV in the chamber in case of unscheduled power outages. Before assembling, the vacuum components are first individually washed in acetone, ethanol and methanol baths in a sonicator and then air baked. After assembly, the chamber is baked again using a heater tape wound around the chamber at 200 C for 4-5 days. Care is taken to avoid any direct heating of the viewports as it leads to melting of the metal-glass seal.
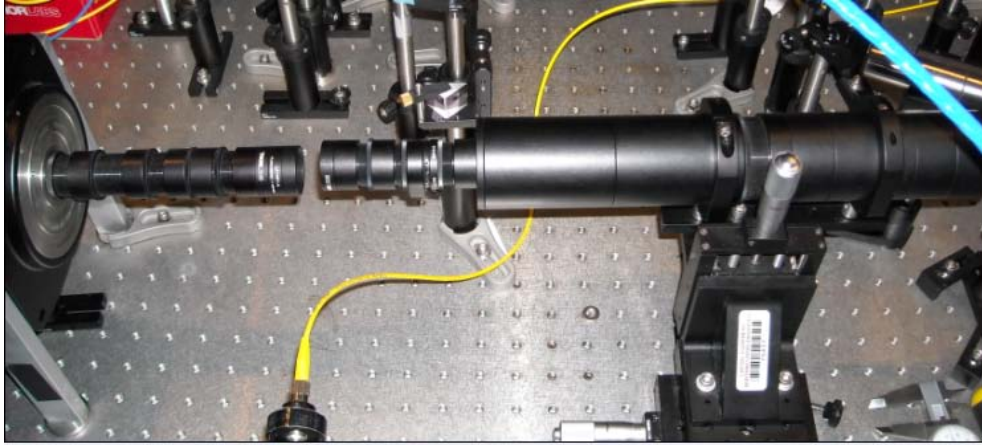
Figure 1.9.   Assembly of the imaging optics and the camera.

1.4. Cooling ions

The ions loaded into the trap via two-photon ionization have temperatures close to the thermal source i.e the oven temperature. Repeated absorption of red-detuned laser photons leads to Doppler cooling of the ions' temperature in a particular direction. This is because the direction of the atomic recoil during absorption is always in the direction of the incident photon whereas the recoil averages to zero during de-excitation via spontaneous emission.. In ion traps, unlike the traps for neutral atoms, the red-detuning need not be ramped up. The ions' oscillatory motion leads to a range of detunings we can address for cooling [10]. In the process of cooling, these atomic ions and any co-trapped molecular ions undergo a phase transition from a liquid to a Wigner crystal when their thermal energy becomes sufficiently small compared with their Coulomb interaction energy [14]. The fluoresence from the atomic ions (^{138}Ba$^+$ in our case) is localized around individual sites as shown in Fig. 1.8a. The relevant closed-cycle transition used to cool ^{138}Ba$^+$ to form such crystals is given in Fig. 1.5b. The linewidths and saturation intensities are 15.17 MHz and 2.6 mW/cm^2 for the $6S_{1/2}$ to $6P_{1/2}$ transition, and 4.93 MHz and 0.374 mW/cm^2 for

the $6P_{1/2}$ to $5D_{3/2}$ transition. The branching ratio is 3:1 for the $6P_{1/2}$ to $6S_{1/2}$ vs $6P_{1/2}$ to $5D_{3/2}$ decay. The power and detuning of the blue (Toptica TA-SGH110 ECDL with doubling cavity) and red (Toptica Pro 100 ECDL) lasers are controlled by using AOMs (acousto-optic modulators) in single and double pass configurations respectively.

1.5. Detecting ions using EMCCD camera

Our imaging system, as shown in Fig. 1.9, consists of two sets of lenses with diameters 1" and 2" mounted on lens tubes. Two different diameter sets have been used in this setup to maximize the light collected from the ions and to accommodate the camera's 1" diameter optic requirements. The primary 2" objective (p/n: AC 508-080-A) has a f/d= 1.376 and a NA of 0.581. The image is focused on to a Princeton EMCCD camera having 512 x 512 pixels with each pixel measuring 16μm x 16μm. The camera is aligned perpendicular to the imaging plane using the spacing between ions as described in Chapter 2. It is operated at a gain of 200 and exposure time of 300ms. Care is taken to avoid direct UV light getting focused on the CCD array. The depth of focus of the objective lens is 0.7mm. Each pixel corresponds to 1.67 microns in the plane of the ions.

1.6. Conclusion

In this chapter, the basics of making, trapping, cooling and imaging ions have been discussed. To make ions, the neutral atomic beam has to be overlapped with the lasers used for ionization inside the trap. For trapping, it is important to know the range of parameters where the ion of interest is stable for the trap specifications. To cool the ions, lasers have to be red-detuned with respect to the resonance and locked to within a few MHz. In order to image the ions, apart from the alignment to image the center of the trap, the depth of field of the imaging system has to be calibrated precisely.

CHAPTER 2

Atomic Thermometry through Imaging

2.1. Introduction

Laser cooled atomic ions, either by themselves or with co-trapped molecular ions, form ordered structures in ion traps as discussed in the previous chapter. The fluorescence images of these atomic ions contain a wealth of information ranging from the trap characteristics [15] and temperature of the constituent ions [16], to the chemical constitution and internal structure of the co-trapped molecular ions [17–19]. Temperatures of these ions are directly measured either by fitting the fluorescence line profile to a Voigt function [20,21], imaging the ion's spatial width in the case of a single ion [22,23] or inferred from a molecular dynamics simulation (MD) [24]. The method of imaging the ion's spatial width measures the Gaussian spatial distribution of fluorescence emitted by ions trapped in a harmonic potential undergoing Brownian motion due to photon absorption [25–27]. Aside from the point-spread width from the imaging optics [28], this Gaussian contains the width arising from the finite temperature of the ion; here the temperature is defined as the time-averaged thermal energy of a single particle divided by the Boltzmann constant [22,23]. Using high magnification optics ($\sim$100), this technique has previously yielded sub-mK precision for temperature measurement on a single ion [22]. In this chapter, the formalism for deriving the temperature of individual ions in a linear Coulomb crystal by relating their spatial spreads to classical normal modes of vibration of a string of ions along with data supporting this technique have been presented.

2.2. Apparatus
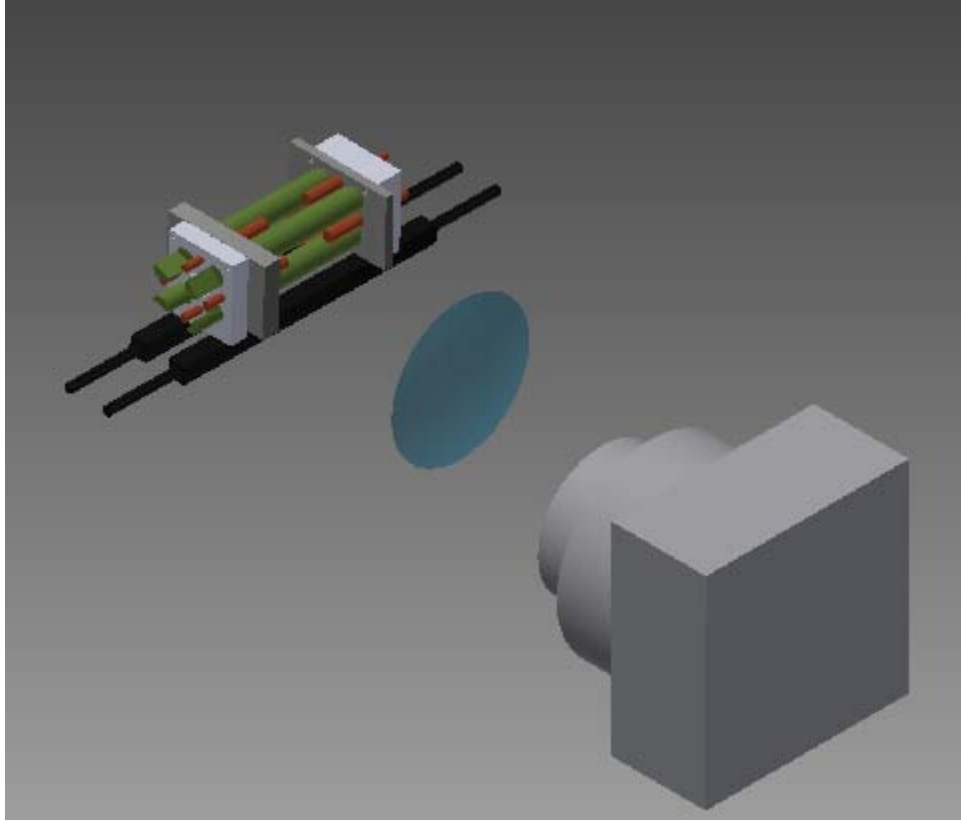
Figure 2.1.   Schematic of the experimental setup. Light from the ions is focused by a series of lenses onto a Princeton EMCCD camera.

Our experimental setup consists of a linear Paul trap of dimensions $2z_0 = 17.8$mm and $r_0 = 3.8$ mm housed in a UHV chamber as discussed in Chapter 1. A Ba^+ cooling laser at 493nm overlapped with a repump laser at 650nm run along the axis and at $45°$ to the imaging axis to Doppler-cool the ions along all three axes. Light from the fluorescing barium ions is focused using a series of 1" and 2" imaging optics on to a EMCCD camera having 512 x 512 pixels with a pixel size of 16 μm x 16 μm. The distance between the trap electrodes subtends an angle of $\sim$19 degrees for light collection which is efficiently used by our collection optics (NA $\sim$ 0.45) placed 2.75" from the trap center. The optical

system is calibrated by measuring the distance between the ions' centers and comparing to the theoretical centers calculated in [**29**]. A series of such calibration curves similar to Fig. 2.2 at different dc voltages yields a consistent value of 1.67 microns per each pixel in the EMCCD with our current optics.
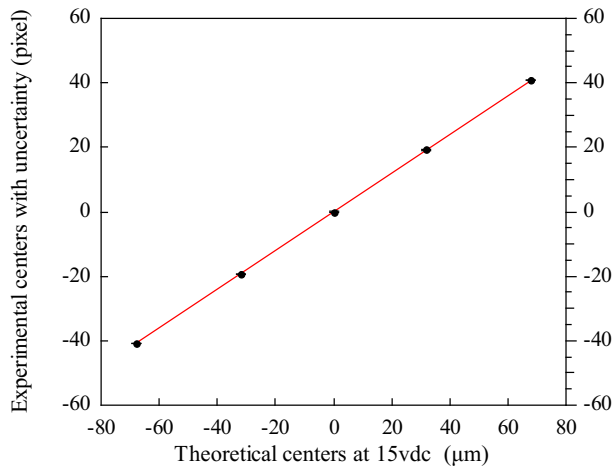
Figure 2.2. Pixel to micron calibration of the optical system using the spacing between ions. The measured positions of centers along with their uncertainty is plotted against theoretical centers calculated using [**29**].

The EMCCD camera is run at a gain of 200 and the exposure time is set to ∼800ms at -70 C. Data is collected from the region of interest and binned along the axis of the trap. Each exposure yields a multi-Gaussian corresponding to the number of ions in the string as shown in Fig. 2.3. The width is extracted from the derivative of this data since the first derivative cuts out any lens blurs and background scatter occurring in imaging. Every data point in Figs. 2.4, 2.5, 2.6, 2.7 is an average of about five hundred such exposures.

2.3. Temperature measurement

The Doppler cooling limit on temperature (T) for a transition of linewidth Γ is given by T$= \frac{\hbar\Gamma}{2k_B}$. In the weak binding limit, where the linewidth of the laser cooling transition
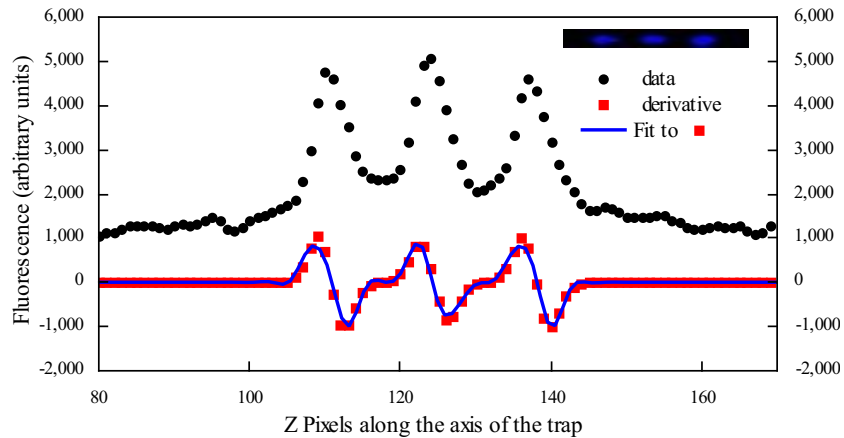
Figure 2.3. Typical fluorescence image of a 3-ion string is shown in the inset. Binned fluorescence (black dots) at each Z pixel gives a multi-Gaussian profile along the trap axis. Spatial derivative of this multi-Gaussian fluorescence signal (red dots) is fit to the multi-Gaussian derivative (blue line) to extract the width of each Gaussian.

(Γ) is much greater than the frequency of the harmonic trap (ω), making $k_B T/\hbar\omega \gg 1$, the time averaged occupation number in the harmonic oscillator is high and is given by $\overline{n} \approx k_B T/(\hbar\omega)$. The spatial distribution of fluorescence of the atom in such cases can be expressed as the product of probability of absorption of a photon (P_n) multiplied by the square of the vibrational wavefunction solution of hermite polynomial for a harmonic oscillator, yielding a Gaussian position distribution as observed in [22]. In addition to this width from temperature, the observed spatial width also contains a contribution from the point spread function (PSF). The PSF is the minimum width arising in any focusing optics due to the fact that a finite cone of light collected from a point source is focused only to a finite disc [28].

The imaged time-averaged spatial distribution of fluorescence from the ions with width $\triangle z$ and center z_0 is given by

(2.1)
$$f(z) = \sum_{n=0}^{\infty} P_n |\psi_n(z)|^2 = \frac{1}{\sqrt{2\pi}\triangle z} e^{\frac{-(z-z_0)^2}{2\triangle z^2}}.$$

where

(2.2)
$$\triangle z^2 = \triangle z_{th}^2 + \triangle z_{PSF}^2.$$

In the case of a single trapped ion, the thermal width comes only from the single mode of oscillation of the ion. In the weak binding limit, this yields

(2.3)
$$\triangle z_{th} \approx \sqrt{\frac{k_B T}{m\omega^2}}.$$

For a finite number of ions p in a string, the width has contributions from all the normal modes of vibration of ions in a harmonic potential coupled via Coulomb interaction. In this case, the Gaussian width in Eq. 2.1 for each ion has contributions from all the p modes the string can vibrate in, each appropriately weighted by the component of the eigenvector of that mode.

(2.4)
$$\triangle z^2 = \Sigma_{p-modes}\{\triangle z_{th_p}^2\} + \triangle z_{PSF}^2.$$

(2.5)
$$\triangle z_{th} = \sqrt{S_1 \times (k_B T/m\omega_1^2) + S_2 \times (k_B T/m\omega_2^2) + ...};$$

where $S_1 + S_2 + ... + S_P = 1$. This equation can also be rewritten in terms of the center of mass frequency (ω_{COM}), denoted by ω_1 in the equations above, since the frequency of all the higher modes can be expressed in terms of ω_{COM} [29]. The COM axial frequency of the

crystal is given by Eq. 2.6, where m is the effective mass of the crystal, $2z_0$ is the distance between the endcaps, κ is the geometric factor for the trap, Q is the effective charge of the crystal and U_{dc} is the voltage on the endcaps.

$$(2.6) \qquad\qquad 1/\omega_{COM}^2 = m \times z_0^2/(2\,\kappa\,Q\,V_{ec})$$

Rewriting Eq. 2.5, we express the width as

$$(2.7) \qquad\qquad \triangle z = \sqrt{\triangle z_{PSF}^2 + \gamma^2(k_B T/m\omega_{COM}^2)}$$

with γ calculated for strings upto 10 ions in Table 2.3. For a single ion, $\gamma = 1$, and in the case of a three-ion string, the γ values are 0.7271, 0.6695 and 0.7271 for the left, center and right ion respectively. As seen from these values and also from Eq. 2.7, the farther an ion from the center of the string, the larger its spatial spread. In the case of a 3-ion string, Fig. 2.4 shows how the center ion has a smaller width than the end ions.
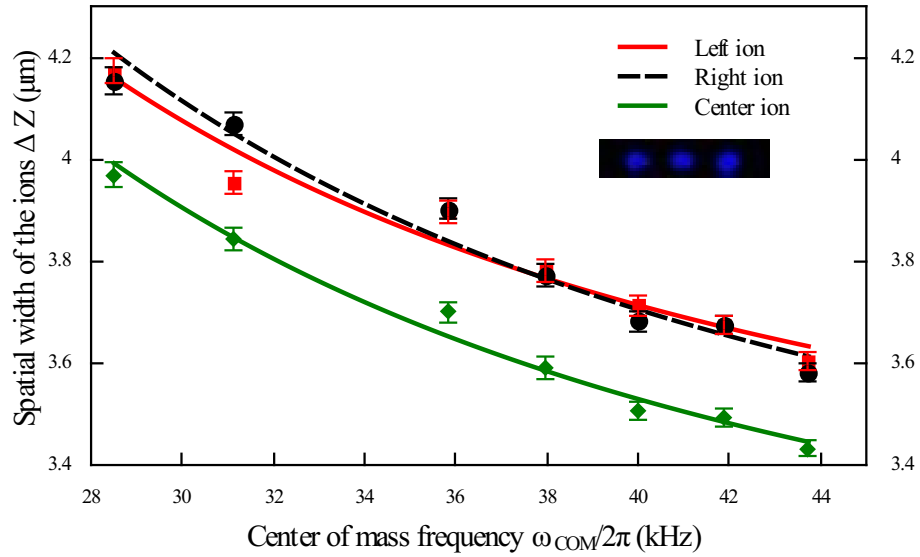
Figure 2.4. The measured spatial widths of the ions from the fluorescence image follow the relationship given by Eq. 2.7 with the width of center ion being smaller than the one on the edges. The temperature of the first, second and third ions are extracted to be 7.18 ± 0.70 mK, 8.41 ± 0.51 mK and 8.15 ± 0.71 mK. The error bars are the 1σ measurement errors in the widths measured from 500 images for each data point.

p-ions	γ_1	γ_2	γ_3	γ_4	γ_5	γ_6	γ_7	γ_8	γ_9	γ_{10}
1	1	-	-	-	-	-	-	-	-	-
2	0.8164	0.8164	-	-	-	-	-	-	-	-
3	0.7271	0.6695	0.7271	-	-	-	-	-	-	-
4	0.6703	0.5975	0.5975	0.6703	-	-	-	-	-	-
5	0.6297	0.5514	0.5340	0.5514	0.6297	-	-	-	-	-
6	0.5985	0.5183	0.4933	0.4933	0.5183	0.5985	-	-	-	-
7	0.5734	0.4928	0.46440	0.4562	0.4644	0.4928	0.5734	-	-	-
8	0.5527	0.4722	0.4414	0.4293	0.4293	0.4414	0.4722	0.5527	-	-
9	0.5350	0.4551	0.4234	0.4085	0.4042	0.4085	0.4234	0.4551	0.5350	-
10	0.5197	0.4405	0.4079	0.3917	0.3848	0.3848	0.3917	0.4079	0.4405	0.5197

Table 2.1. Table of γ_x values for ions in different x positions of a string using Eq. 2.5 and Ref. [29].

2.4. Results
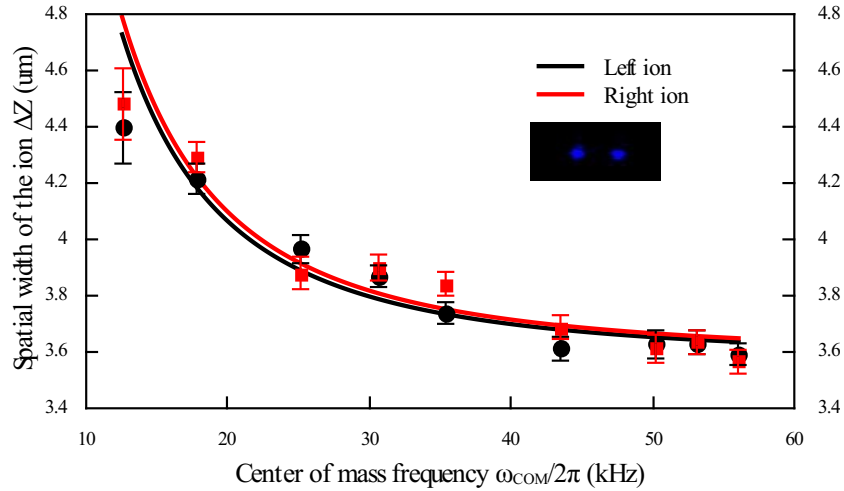
Figure 2.5. In this 2-ion string data, widths of the left and right ion follow the expected curve of Eq. 2.7. Temperatures are extracted to be 1.49 ± 0.30 mK and 1.57 ± 0.28 mK for the left and right ion respectively.
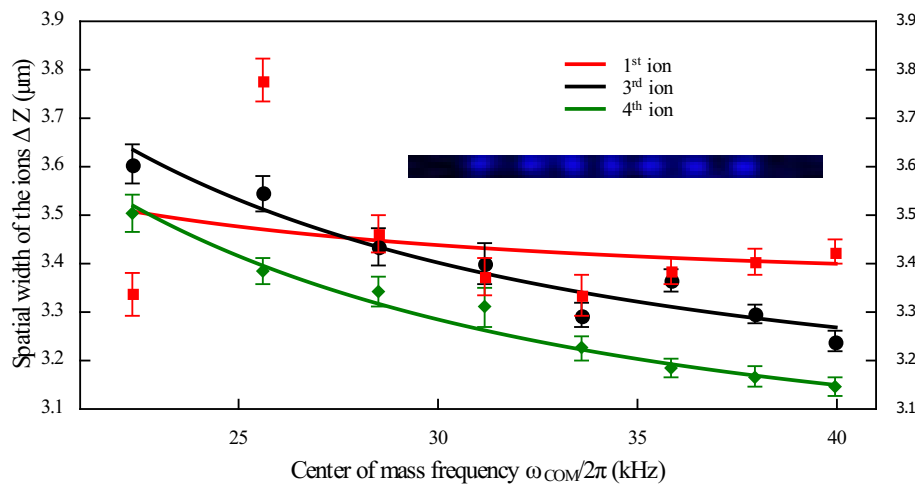
Figure 2.6. Ions closer to the center in a 7-ion string follow the expected curve of Eq. 2.7 whereas the ion at the end does not. Temperature of the 3rd and 4th ions are extracted to be 5.58 ± 0.82 mK and 5.63 ± 0.33 mK respectively.
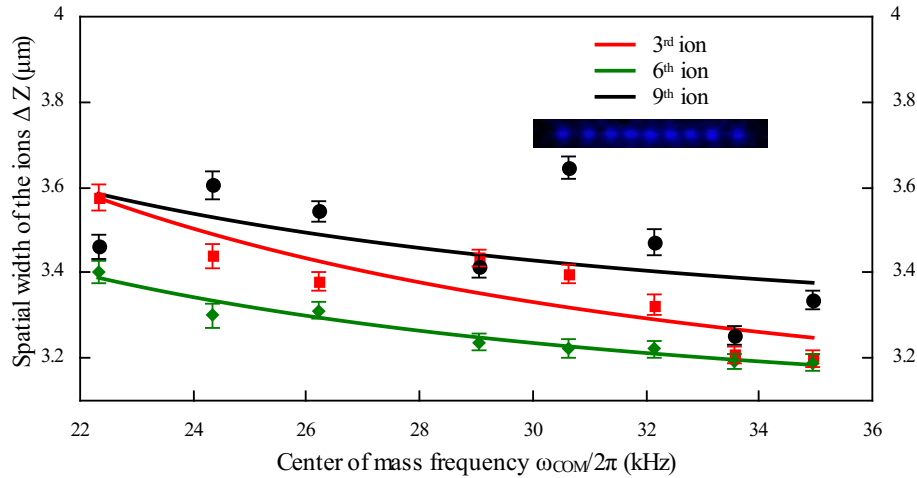
Figure 2.7. In this 9-ion string data, the ions closer to the center ((e.g the 6th ion) follows the expected curve of Eq. 2.7 whereas the ions closer to the ends do not. Temperature of the 6th ion is 5.57 ± 0.78 mK.

Temperature measurements on a string of ions have lower precision compared to single ion experiments [25], because of the comparatively lower magnification required to image all ions at once. In the case of a three-ion-string, all the ions fall on the curve according to Eq. 2.7 yielding temperatures of 7.18 ± 0.70 mK, 8.41 ± 0.51 mK and 8.15 ± 0.71 mK for the first, second and third ions respectively (see Fig. 2.4). Data for a two-ion string is shown in Fig. 2.5. For longer strings, the center ions follow the curve predicted by Eq. 2.7 but the ions further out deviate from this prediction as can be seen in Figs. 2.6 and 2.7. Possible reasons for this could be the difficulty in maintaining the alignment of the camera perpendicular to large strings through all the different applied endcap voltages (as local patch potentials can cause bending in ion strings), and the effect of anharmonic terms in the potential experienced by ions farther from center.

2.5. Conclusion

In summary, we have discussed the formalism for determining the temperature of individual ions in a linear Coulomb crystal via fluorescence imaging of their spatial spreads. We experimentally show that the method is applicable for all the ions in small strings (3 - 4 ions), and for ions close to the center in large strings (up to 10 ions). This technique offers an alternate method to the traditional fluorescence line profile measurements, which require the knowledge of the laser-cooling rate's dependence on detuning for accurate temperature determination [20, 21]. Our method also offers better accuracy (<1 mK) compared to molecular dynamics simulations based on crystal geometry (<10 mK) [24].

CHAPTER 3

Molecular Ion Production and Detection Techniques

3.1. Introduction

Trapped molecular ions in linear Paul traps, like atomic ions, have long trapping times of hours independent of their internal state. Though Doppler cooling of molecules is harder due to their complex internal structure, their Coulomb mediated interaction with co-trapped laser cooled atomic ions leads to sympathetic cooling of their external degrees of freedom. In this chapter, details of our apparatus for producing molecular ions in ion traps and a mass determination technique for identifying the produced molecular ion will be discussed. Traditionally, molecular ions in ion traps are produced by leaking in neutral gas with a measurable back-ground pressure as determined by a local ion gauge [30, 31]. Recent experiments involving overlap of neutral atoms trapped in a MOT (magneto-optical trap) with trapped atomic ions [32] or directed jets from a pulse-valve have also deterministically produced molecular ions [33]. Directed jets from pulse-valves provide high particle densities compared to simply leaking in a gas, increasing the probability of a reaction. They also offer much simpler experimental setups as compared to MOTs. Our apparatus employing a pulse valve allows us to maximize the flow of reactant gas at the site of the ionic crystal while keeping the overall pressure in the chamber low, along with fast pump out times. The molecular species produced after each burst of gas is determined by exciting the collective vibrational mode of the two-species string via an rf voltage applied to the endcaps. The frequency of this secular resonance is determined by a Lorentzian fit to

the measured spatial widths in the fluorescence images of the co-trapped atomic ions as a function of frequency. Finally, a potential approach to identifying molecular ion species by measuring the shift in the equilibrium positions of co-trapped atomic ions in a string is also explored.

3.2. Apparatus
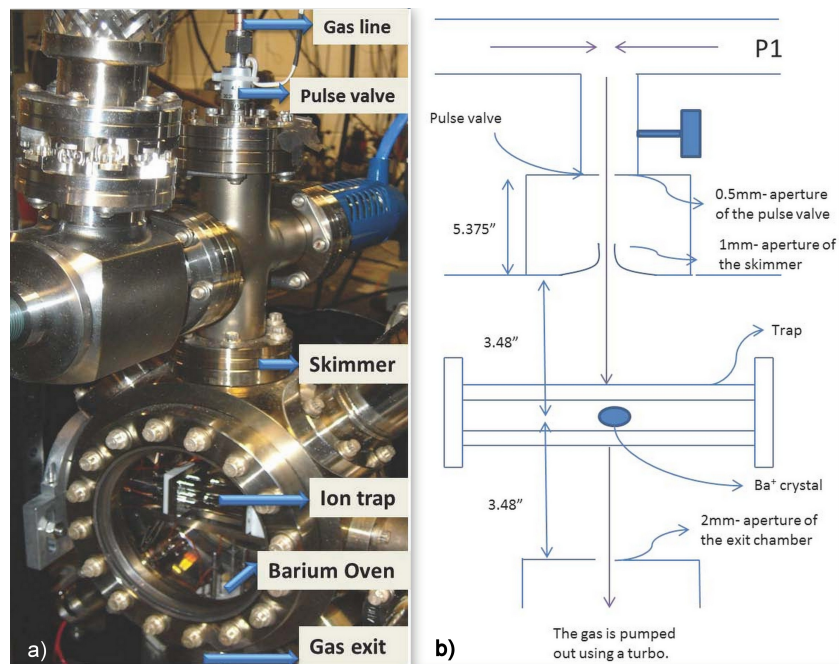
Figure 3.1. Picture (a) and schematic (b) of the experimental chamber.

A gas line consisting of a solenoidal pulse valve (p/n: 009-0442-900- Parker) with a typical backing pressure of 4-8 psi is appropriately positioned to have a line of sight to the trapped ions in the chamber as shown in Fig. 3.1. The pulse valve is operated using a Labview® program that controls electronics (relay switch [p/n: EDR82781/3] and 350 V power supply) to open and close the valve for a minimum period of $200\mu s$ at a maximum frequency of 20 Hz. Between the valve and the ion trap, a 1mm aperture skimmer (see Fig. 3.2) attached to the differentially pumped chamber, skims out the directed jet making

a narrow stream directed to center of the trap. The gas molecules not interacting with the ions and not scattered by the rod electrodes are pumped out using a turbo connected to the 2mm aperture gas exit chamber. Typical pump out time for this setup is around a second as shown in Fig. 3.3. The local density for a duration of 100ms at the center of the trap varies between 10^{11} molecules/cm^3 to 10^{12} molecules/cm^3 . This density is deduced from comparing the reaction rates between N_2O and Ba^+ for our setup (1 reaction/pulse) with that given in [31]. The minimum open time for the valve set by the mechanical response of the armature in the pulse valve is typically 100ms [34].
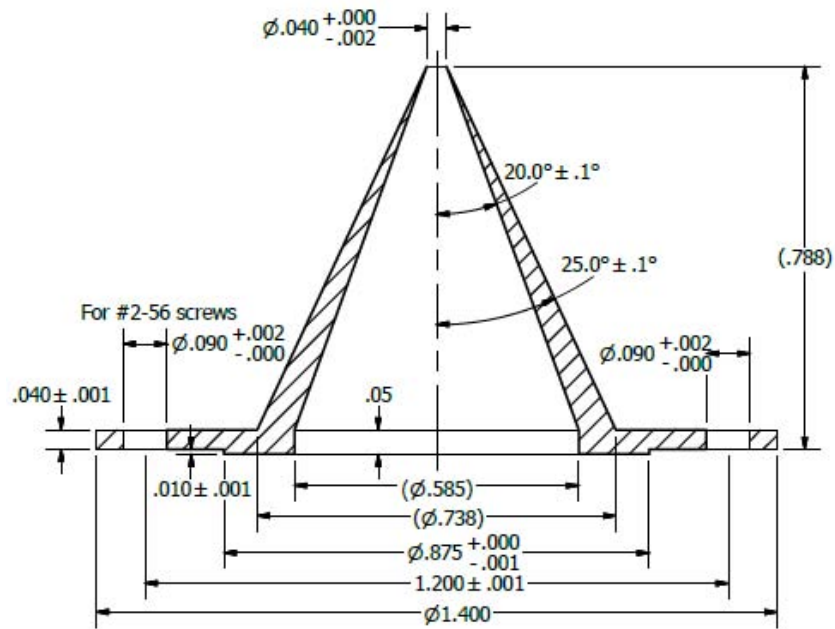
Figure 3.2. CAD drawing of the skimmer used between the pulse valve and the trapped ions.

3.3. Molecule identification

The molecular ion produced in the trap as a result of barium ions reacting with the gas jet is identified by the dark sites in the string. Images of this string are recorded as the frequency of a sinusoidal voltage applied to one of the end caps is varied as shown in Fig. 3.4.
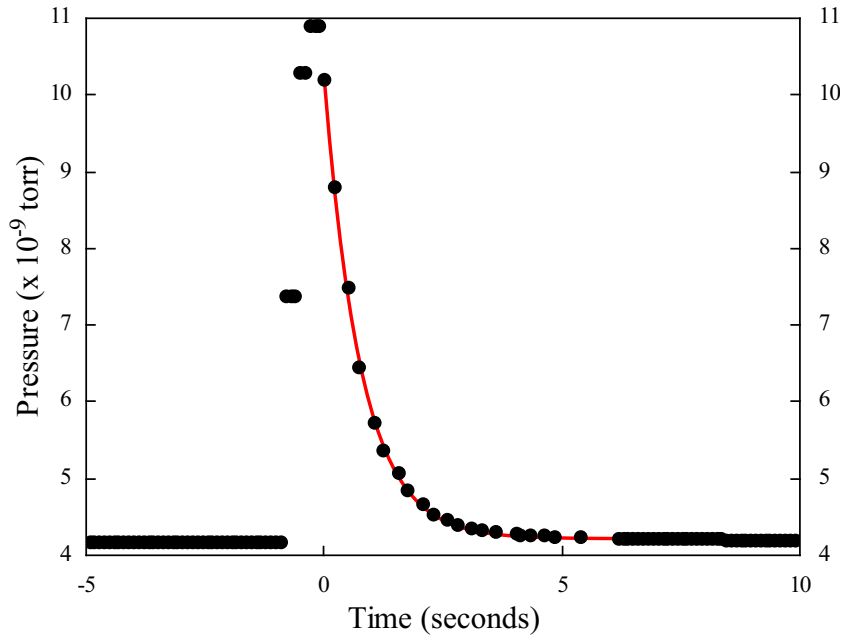
Figure 3.3. Pump out characteristics of N_2O bursts at a backing pressure of 5 Psi as recorded using an ion gauge. Black dots are experimental data and the red line shows exponential fit with time decay of 1 second to the trailing end of gas pumped out.

For an applied drive frequency far away from the center of mass (COM) resonance frequency of the string (ω_{COM}), ions are well localized and bright; closer to resonance, the ions heat up and hence appear dimmer and more spread out, as shown in the Fig. 3.5. The change in position of the bright ions from the on-to-off-resonance images is because of hopping of the dark ions between sites due to radiation pressure and trap imperfections [35] [36]. The average spatial spread of the bright laser-cooled ions are extracted as the drive frequency is varied using a multi-Gaussian fit as described in Chapter 2. The frequency of the COM resonance (ω_{COM}) is determined from a Lorentzian fit to the average width versus frequency curve (see Fig. 3.6). The molecular species is then identified from the shift in the position of the resonance as the composition of the crystal changes, as described below.
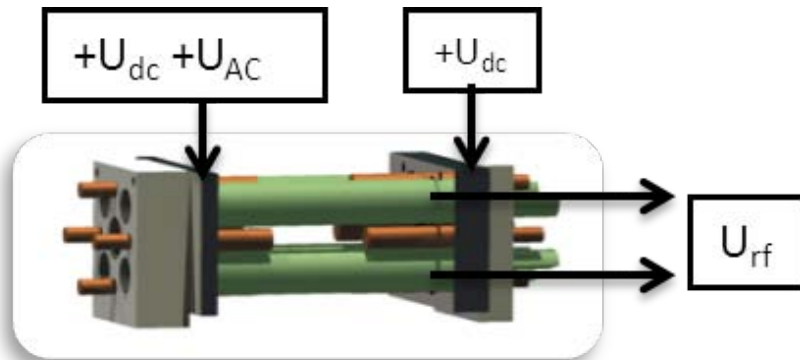
Figure 3.4. Configuration of potentials on the trap electrodes. An rf voltage is applied to one of the endcap electrodes.
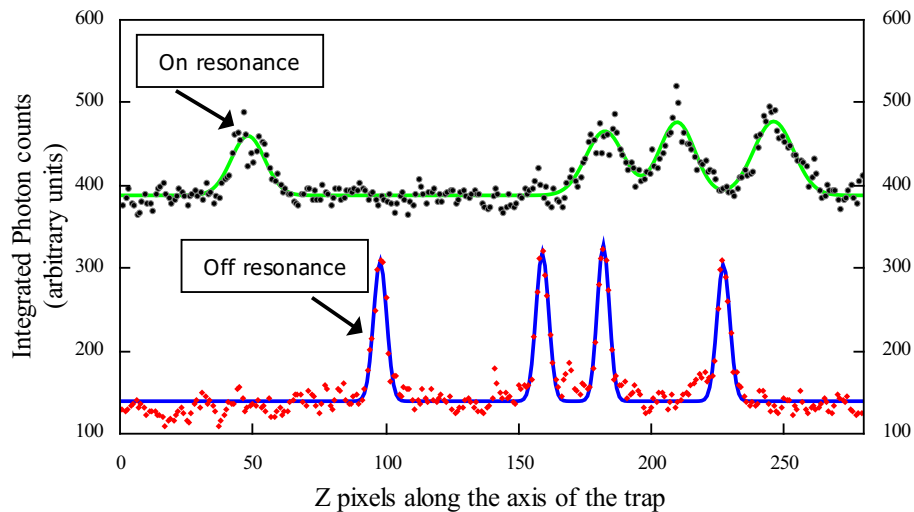
Figure 3.5. Ions when excited with an rf voltage whose frequency is far from resonance are well localized and brighter compared to when excited closer to resonance. The on- and off-resonance images are taken with the same string; the ions appear at different positions because of hopping of the non-fluorescing ions. The two curves are offset vertically for clarity.

The COM axial frequency of the crystal is given by Eq. 3.1, where m is the effective mass of the crystal, $2z_0$ is the distance between the endcaps, κ is the geometric factor for the trap, Q is the effective charge of the crystal and V_{ec} is the voltage on the endcaps.

(3.1)
$$1/\omega_z^2 = m \times z_0^2/(2\,\kappa\,Q\,V_{ec})$$
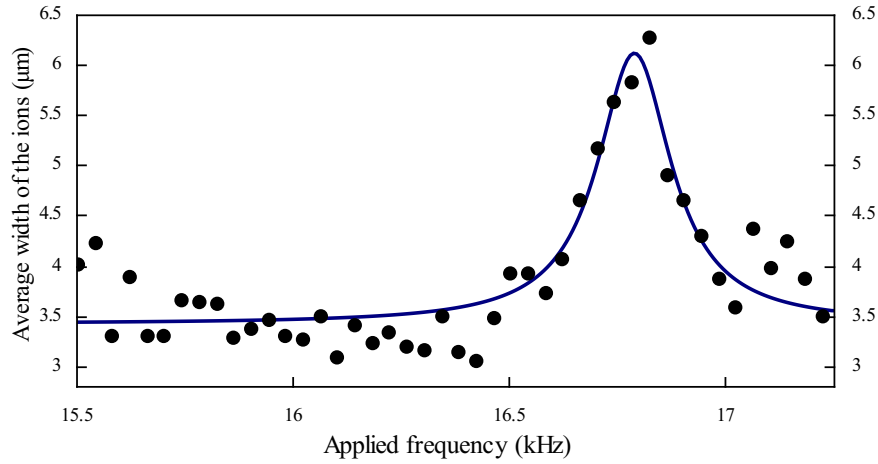
Figure 3.6. Lorentzian spatial width response of the ions to a driven oscillation via an rf voltage applied to the endcaps. The spatial spread of the ions increases closer to COM mode resonance frequency due to heating, whereas away from resonance the ions are more localized.
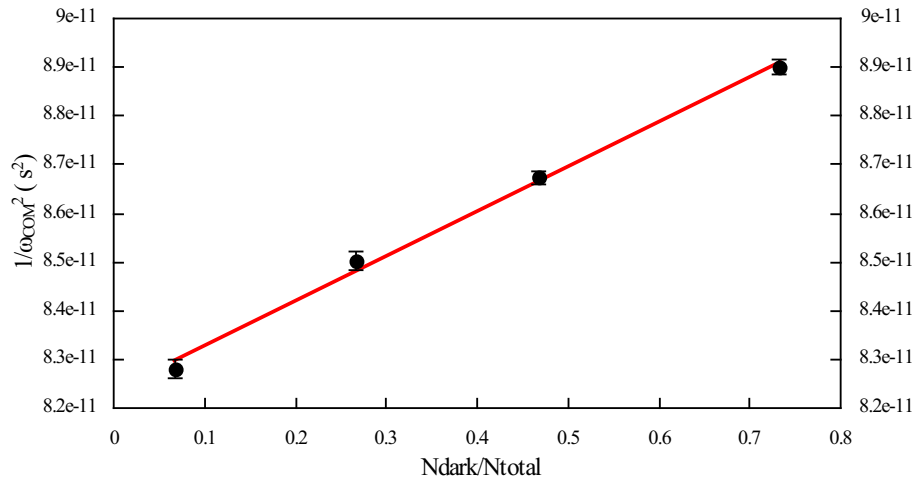
Figure 3.7. The linear fit according to Eq. 3.2 from the measured frequency response of a bi-crystal yields a mass of 15.40 ± 0.76 amu for X in BaX$^+$, identifying the molecular ion as BaO$^+$.

In the case of a bi-crystal with Ba$^+$ and BaX$^+$, Eq. 3.1 becomes

$$(3.2) \qquad 1/\omega_{COM}^2 = \{m_{Ba} + Ndark \times m_X/Ntotal\} \times z_0^2/(2\,\kappa\,Q\,V_{ec})$$

where Ndark/ Ntotal is the fraction of dark ions in the crystal. We resonantly excite the crystal after its composition is changed after each burst of gas to get a response similar to Fig. 3.6 in each case. Taking an average of 20 such measurements after every burst, we obtain the data shown in Fig. 3.7. From the ratio of the slope to the intercept, mass of the atom "X" in the molecular ion "BaX^+" is identified. Since this method eliminates any error involved in the knowledge of other trap parameters, it leads to a high precision ($<1\%$) mass determination. The determination of the secular resonance frequency in Fig. 3.6 can equivalently be realized at higher drive voltages by measuring the change in integrated fluorescence of the ionic crystal as the drive frequency is varied. However, this method does not provide position information since at high voltages, close to resonance, the ions in a string become highly delocalized.
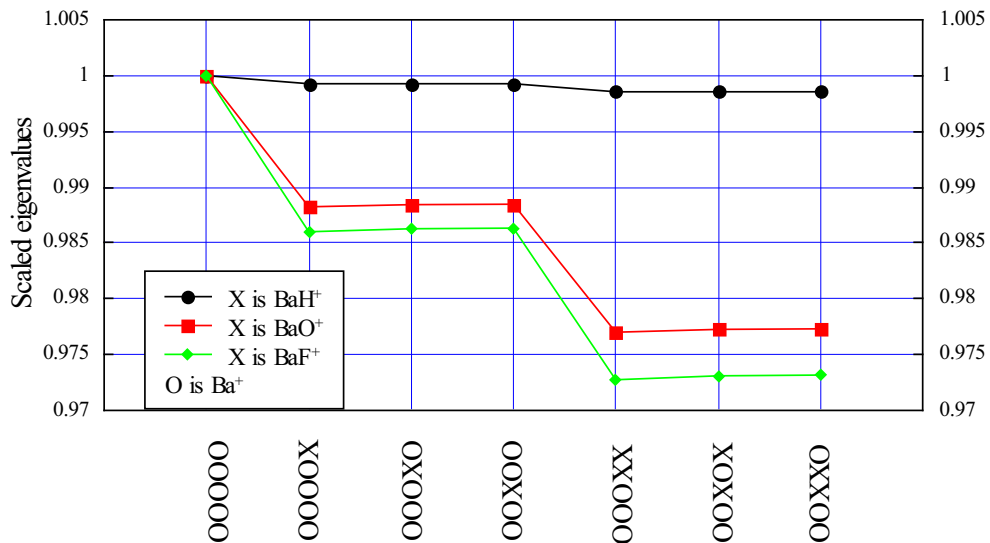
Figure 3.8. Shifts in positions of the Ba^+ ions (o) as the molecular ion (x) hops to different positions in the string. Since all the ions are moving in the direction of the cooling laser, shift due to any pseudo potential gradient must be very small compared to the radiation pressure force.

Extensions of our technique for measuring frequencies other than the COM mode requires that the shifts in resonant frequency caused due to hopping of the molecular ion are well separated from those resulting from the change in composition of the crystal itself [**33**, **37**]. In the case of the COM mode, these configurational shifts are negligible compared to the compositions as can be seen in Fig. 3.8. Amongst the three species compared, BaH^+ shows the least variation. Since our technique has a resolution of ≈ 1 KHz for typical parameters, it is not possible to identify BaH^+ using this method. The numerically calculated eigenvalues plotted in Fig. 3.8 use mass weighted co-ordinates as prescribed in [**33**, **37**].

3.4. Shifts in ion positions

Another technique proposed for ion detection uses the shift in equilibrium positions of the co-trapped atomic ions as the molecular ion moves from one site to another [**39**]. Since our imaging technique gives us a precision of 1% in determination of the center of the average ion position, we looked for shifts in the position of the bright ions as the dark ion hopped to different positions in the string. The competing effects that shift the equilibrium position of the ions are the optical radiation pressure force arising from the resonant scattering of photons by the laser-cooled ions, the psuedo potential gradient arising due to finite size of the rf rods and any anharmonicity in the trapping potential. Anharmonicity is significant in smaller traps and in regions away from the trap center. Since the ions are on axis in a large trap, this effect is not significant in our case. Pseudo-potential gradients lead to shifts in different directions depending on the orientation of the dark ion with respect to the bright ions whereas a shift from radiation pressure force is always in the direction of propagation of the cooling laser. The displacement of barium ions measured

with respect to a pure Ba^+ string are plotted in Fig. 3.9 as the molecular ion jumps from site to site. The laser-cooled barium ions are denoted by "o" and the molecular ion is denoted by "x". Since all the shifts are positive with respect to the direction of propagation of the cooling laser, we conclude that the shifts due to pseudo potential gradient, if at all present, are very small compared to the shift due to radiation pressure force. Since the optical radiation pressure force is independent of the chemical composition of the molecular ion, this method cannot be used to identify molecular ions in our trap.
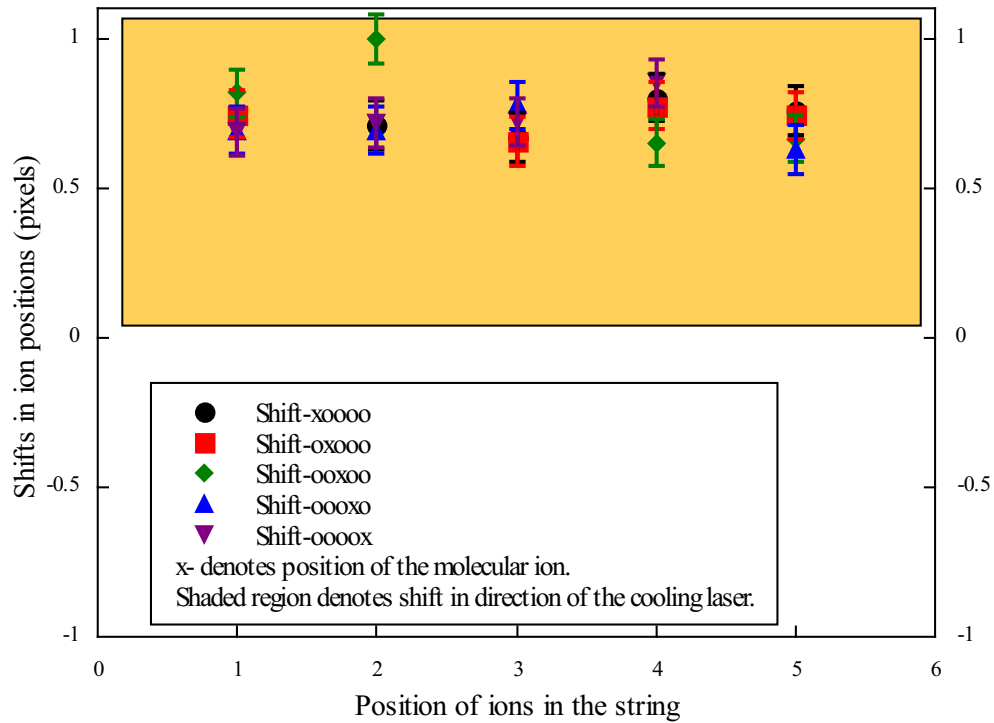
Figure 3.9. Shifts in positions of the Ba^+ ions (o) as the molecular ion (x) hops to different positions in the string. Since all the ions are moving in the direction of the cooling laser, shift due to any pseudo potential gradient must be very small compared to the radiation pressure force.

3.5. Conclusion

In this chapter, we presented an experimental arrangement for making molecular ions without significant increase in background pressure. This could be of interest for future experiments, since it can potentially be used to investigate chemical reactions with small cross-sections. We also discussed a method for molecule identification that does not involve knowing the trap parameters precisely. Furthermore, our molecule production and mass determination techniques are also promising for recyclable spectroscopy, where the pure string of atomic ions is restored after spectroscopy on a particular quantum state of the molecular ions, as will be discussed in the following chapter.

CHAPTER 4

Candidates for Recyclable Spectroscopy and Laser Cooling

4.1. Introduction

Recently developed techniques to access molecular internal degrees of freedom have made molecules promising test-beds for fundamental experiments ranging from the search for a permanent electron electric dipole moment (EDM) and the variation of fundamental constants of nature over cosmic time to the study of ultra-cold chemical reactions [40–43]. Trapped molecular ions are favorable for such experiments offering advantages such as long trapping times independent of the internal state in addition to a well-determined particle number. When co-trapped with atomic ions, the external degrees of freedom of molecular ions can be cooled by Coulomb-mediated sympathetic cooling. However, due to the large distance between the atomic and molecular ions ($\sim$microns) in the trap, the internal degrees of freedom of the molecules remain unaffected. Therefore, in order to access the transitions of interest, molecules are either directly prepared in the state of interest [44], cooled using short-range interactions between the molecular ions and an overlapped atomic MOT (magneto-optic trap) [45, 46] or directly laser-cooled using a reasonably closed-cycle transition [47–49]. In this chapter, two classes of molecules are proposed, one that can be state prepared and another that can be laser-cooled. Further, the energies of the ro-vibrational levels and the cross-section for molecule dissociation are analyzed using Level [50] and Bcont [51] codes respectively.

4.2. Review of 1+1' Resonance-Enhanced Multi Photon Dissociation (REMPD)
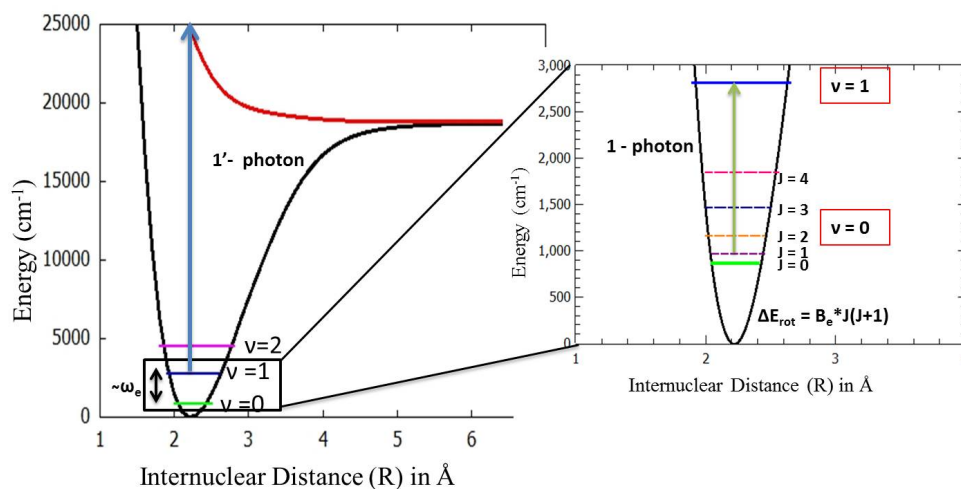
Figure 4.1.   Schematic of the REMPD scheme for state read-out in molecules. 1-photon excites the molecules in a specific rovibrational state to an intermediate state and the 1'-photon resonantly excites the molecule to a dissociative excited electronic state.

Resonance-Enhanced Multi Photon Dissociation (REMPD) derives its name from the resonant single or multiple photons used to excite a molecule to an intermediate state before it is dissociated by an another photon [52]. In order to quantify the efficiency of any molecular cooling or state preparation scheme, a rotational state selective REMPD scheme with atleast two distinct photons (1 and 1') is required. The narrow 1-photon has the tunability to address each rovibrational state and the broad 1'-photon drives the molecule to dissociation as depicted in Fig. 4.1. Figuring out a favorable 1+1' scheme in terms of optical power and wavelength is a part of all experiments that involve internal state manipulation. Typically for diatomic molecules the 1-photon is in the near-mid IR region and 1'-photon in the ultra-violet or blue region of the electromagnetic spectrum.

4.3. Recyclable Spectrosocopy

In this section, a class of favorable molecules for a spectroscopy scheme, referred to as recyclable spectroscopy, will be discussed. This state preparation method provides access to any specific transition of interest by preparing molecules in any chosen rovibrational state. Starting from a string of laser cooled atomic ions, molecules of interest are produced by flowing in an appropriate reactant gas, and after the experiment, the molecules are dissociated back to recycle the string of laser cooled ions we started out with. This scheme works only for experiments with molecules where one of the atoms can be laser cooled and when the molecular dissociation rates are insignificant at the wavelengths used for cooling the atomic ions. By eliminating the need to load a new laser-cooled ion string every run, this proposed state preparation method can be used to decrease the dead time in experiments.

4.3.1. Procedure

The first step of the procedure described below needs to be carried out only once in the beginning of the experiment. Every spectrosocopy cycle yields a Ba^+ string by construction.

Step 1: Load Ba^+.

Step 2: Leak in reactant gas to form BaX^+.

Step 3: Dissociate BaX^+ in the "wrong" state to give Ba^+. By "wrong" here we refer to the molecules in states other than the ro-vibrational state of interest.

Step 4: Do spectroscopy with ions in the desired ro-vibrational ground state and finally dissociate them to make Ba^+.

Go to step 2.

In the case that we form molecules other than those of interest, because of impurities in the reactant gas or from natural BaO^+ formation in the traps, we can dump these undesired heavy ions from the trap by making the trap unstable for higher masses as discussed in Chapter 1. The undesired molecule is always heavier than the atomic ion because charge exchange at typical trap depths of 2-3 eV and laser-cooled temperatures is unlikely.

Candidates

BaH^+. Compared to other molecules, H_2 is harder to pump out of a vacuum chamber because of its small size and high thermal velocity. This leads to undesired formation of BaH^+ in trapped Ba^+ strings. Photo dissociation calculations carried out with the curves given in [53] assuming a constant 1-debye transition dipole moment, gives cross-sections as shown in Fig. 4.2. Though the y-axis gets scaled depending on the actual transition dipole moment, there is a significant probability of dissociation (1 molecule/2 minutes) at the Ba^+ cooling laser wavelength (493nm) with laser powers beyond saturation, ruling out the possibility of BaH^+ being a possible candidate. However, we do occasionally observe fluorescing barium turn dark in the trap and then become bright again after a while. This could be because of possible BaH^+ production in the trap.

BaO^+. The potential energy curves of BaO^+ [54] shows a low-lying electronic state close to the ground state as can be seen from Fig. 4.3. Since any possible 1+1' REMPD scheme will require understanding of this less documented low-lying electronic state, more spectroscopic data is needed to further analyze this candidate molecule.
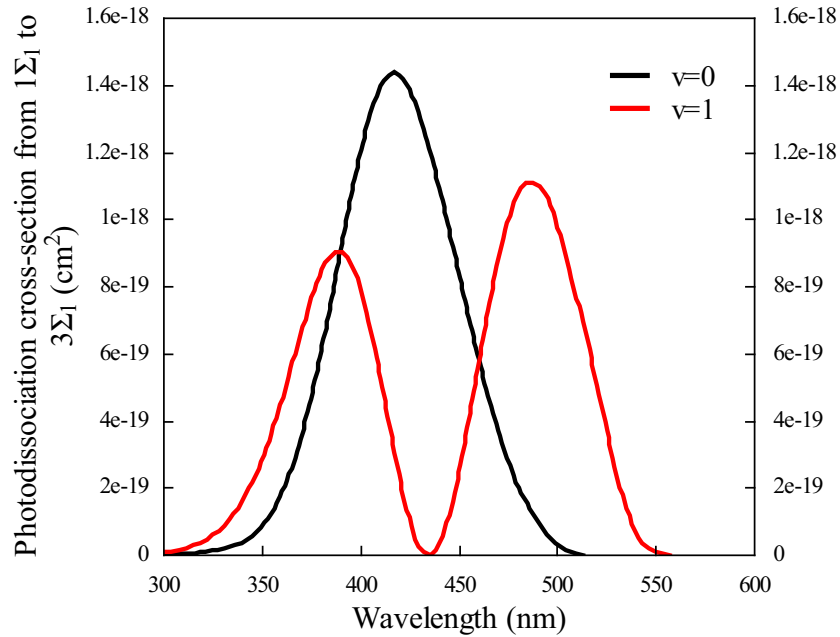
Figure 4.2. Photo-dissociation cross-section for BaH+ is significant at the Ba$^+$ cooling laser wavelength (493nm). This could result in unwanted dissociation of any prepared BaH$^+$.

BaF$^+$

BaF$^+$ [54] has a very deep potential energy curve as shown in Fig 4.4. At room temperature, 92.8% molecules are present in the $v = 0$ ground vibrational level, making this candidate promising. The 1-photon wavelength lies in the 17.9-18.7μm range. For the 1'-photon, though the primary transitions from v=0 are in the deep UV (highest cross-section around 180nm), one can also drive the molecule from higher vibrational overtones with slightly longer wavelengths and higher powers (see 4.5).

BaCl$^+$

Though vibrational cooling of BaCl$^+$ has already been demonstrated in an ion-neutral hybrid trap [46], any transition of interest in this molecule can be driven using our method
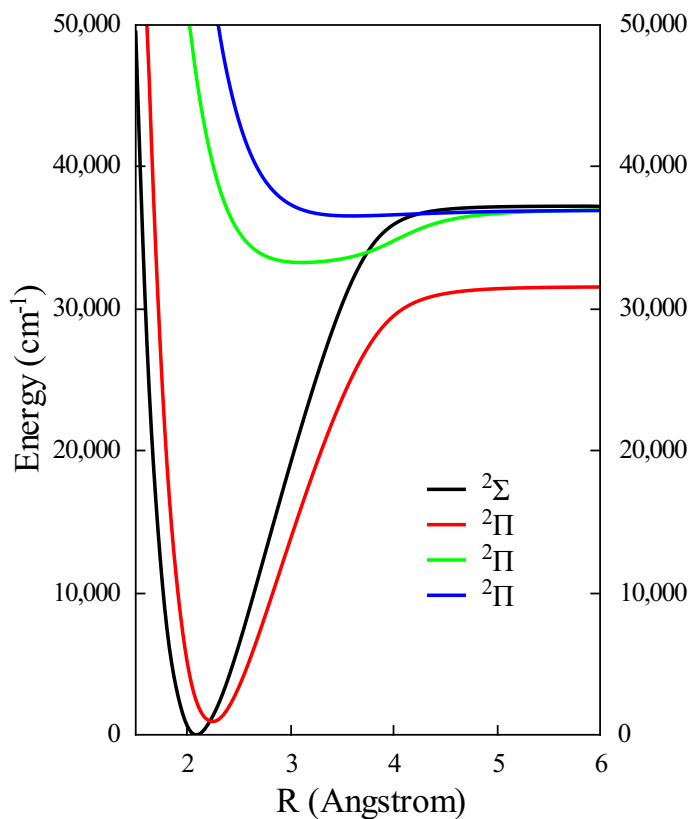
Figure 4.3.   Potential energy curve of BaO^+. The low-lying state close to the ground state has to be understood more thoroughly to determine a REMPD scheme.

without having to cool the molecule. 1'-photon scheme for $BaCl^+$ is shown in Fig. 4.6 with the 1-photon wavelength in the 29.5-30.5μm range.

Molecular Candidates for Rotational Cooling

Any attempt to laser cool a molecule's internal degrees of freedom involves finding a closed-cycle transition scheme with a finite number of lasers to drive the molecule to its ro-vibrational ground state. In this section, analysis on two promising candidates with spin-orbit split ground electronic states will be discussed. Spin-orbit coupling leads to symmetrical splitting of the ground state about the mean position of the nuclei guaranteeing
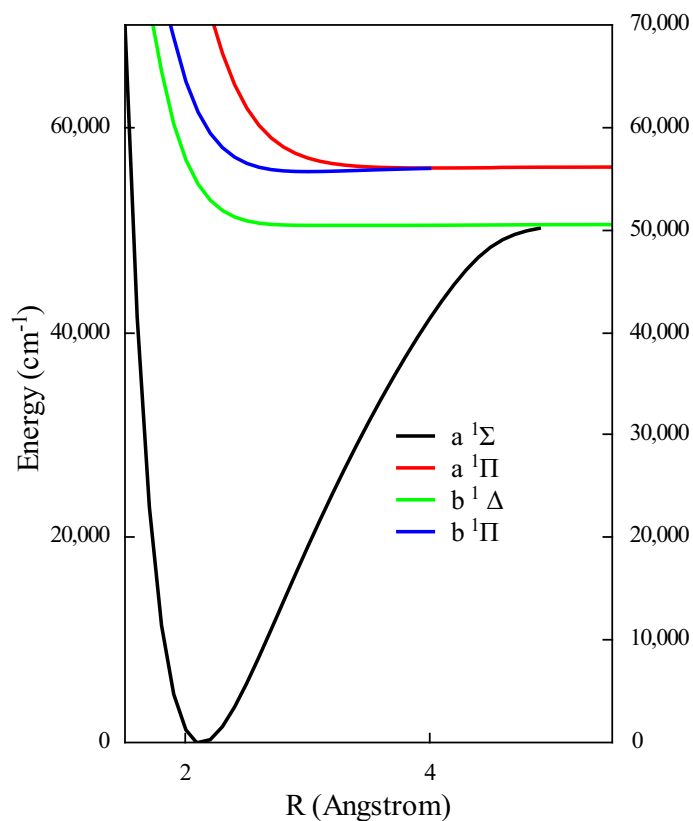
Figure 4.4.   Potential energy curve of BaF$^+$.

a near diagonal Franck-Condon factor (FCF) by construction, a necessary criterion for finding a closed-cycle scheme. The transitions between these states is forbidden without state mixing and hence the transition moments are very low and power requirements to drive these transitions are higher.

In addition to diagonal FCF, candidate molecules also need to have the following

(1) well separated P-Q-R branches [1] to be able to drive the P-branches separately since P-branch excitation leads to decrease in rotational energy in de-excitation.

---

[1]In the simplest of cases where an electronic state has a net orbital angular momentum, like a $^1\Pi$ state, Q branch refers to a vibrational excitation where the change in rotational quantum number is zero ($\Delta J = 0$). P, R branches refer to excitations where $\Delta J = $ -1 and +1 respectively.
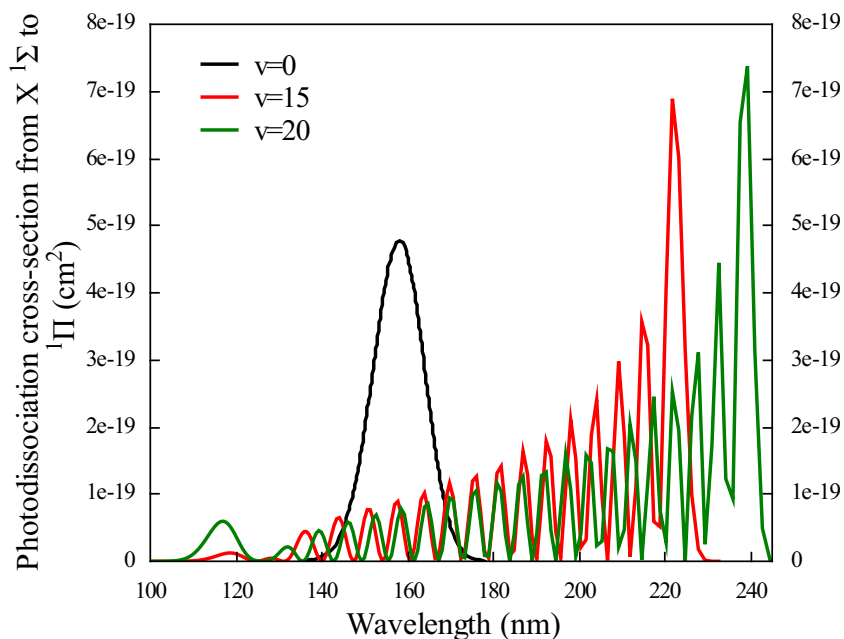
Figure 4.5. 1′-photon scheme for BaF$^+$. Though the primary transition from $v = 0$ is in deep UV, the molecule can be excited to higher vibrational levels (e.g. $v = 15, 20$) from where it can be dissociated using longer wavelength lasers.

(2) transitions that can be driven fast to avoid any redistribution due to blackbody radiation.

(3) dissociation scheme in an accessible wavelength range.

Once the molecule is prepared in the ground state, in order to quantify the efficiency of our cooling scheme we need to have a ro-vibrational selective 1+1' REMPD scheme to destructively count the number of molecules that have been cooled.
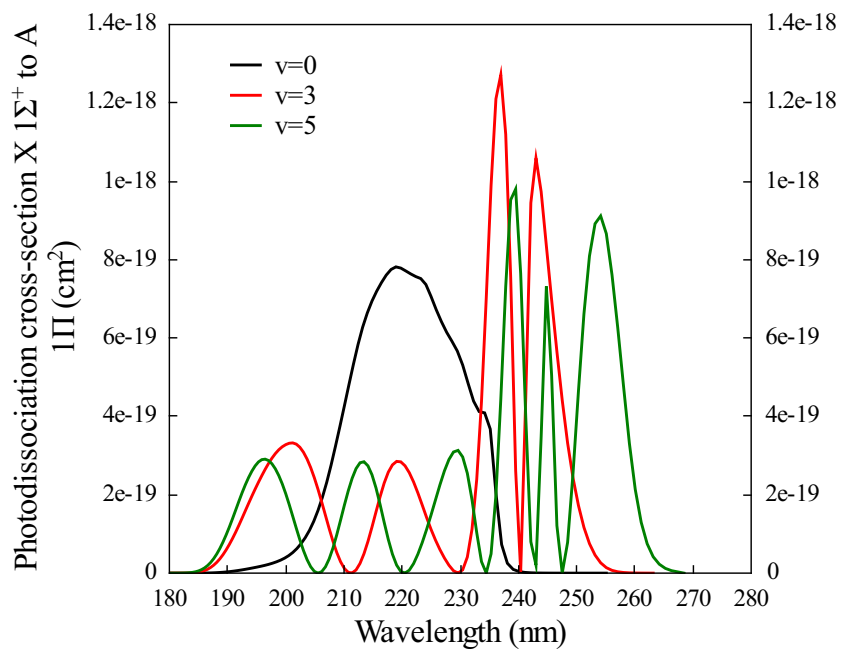
Figure 4.6. 1′-photon scheme for BaCl$^+$. The transitions for dissociating from any of the low vibrational levels ($v = 0, 3, 5$) can be driven using dye lasers.
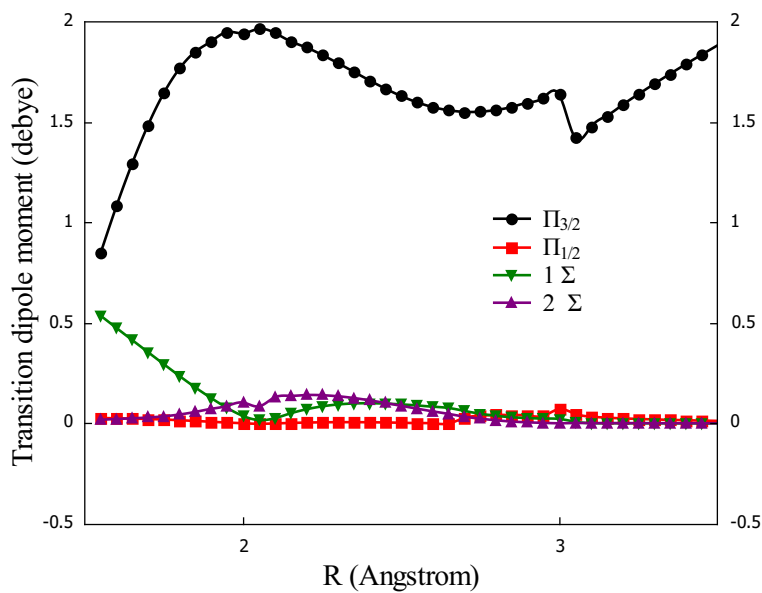
Figure 4.7. Transition dipole functions from X $\Pi_{3/2}$ to the other states in IF$^+$.

	$HI^+(^2\Pi)$	$IF^+(X^2\Pi_{3/2});\ (^2\Pi_{1/2})$	$ICl^+(X^2\Pi_{3/2});\ (^2\Pi_{3/2})$
$w_e(cm^{-1})$	2195.24	696 ; 687	429 ; 437
$w_e x_e(cm^{-1})$	39.60	3.0 ; 1.2	1.35 ; 2.08
r_e (Å)	1.632	1.836 ; 1.832	2.24 ; 2.224

Table 4.1. Table of molecular constants of HI^+, IF^+, ICl^+

Vibrational number	$HI^+(X^2\Pi_{3/2})$	$IF^+(X^2\Pi_{3/2})$	$ICl^+(X^2\Pi_{3/2})$
v" = 0	99.99	96.74 %	77.94 %
v" = 1	0.00	3.15 %	17.03 %
v" = 2	0.00	0.11 %	0.90 %
J_{max} at v" = 0	4	7	33

Table 4.2. Population in the different vibrational levels of the ground state at T=300 K. J_{max} is the rotational number in the ground vibrational where the population distribution peaks.

v" → v'	$IF^+(X^2\Pi_{3/2}$ to $\Pi_{1/2})$	$ICl^+(X^2\Pi_{3/2}$ to $\Pi_{1/2})$
FCF 0 → 0	99.24	95.15
FCF 0 → 1	.73	4.52
FCF 0 → 2	0.02	0.90

Table 4.3. Diagonal Franck - Condon factors between ground v" = 0 $X^2\Pi_{3/2}$ state and excited v' $\Pi_{1/2}$ state.

Candidates

IF^+

IF^+ ($^{127}_{53}$I and $^{19}_9$F)has a spin-state ground Π state with molecular constants given in Table 4.1 [**55**]. The population distribution of the molecule at 300 K is listed in Table 4.2 showing that a signification population of 96.74% is present in the ground vibrational state. As expected in these spin-split molecules as described above, the FCF for any cooling scheme between the $\Pi_{3/2}$ and $\Pi_{1/2}$ states is favorable. The transition rates calculated using Level for the ν" = 0 and ν'=0,1 states are also large. Possible 1+1' scheme calculated using Level and Bcont using the transition dipole function given in Fig 4.7 yield 1-photon wavelengths
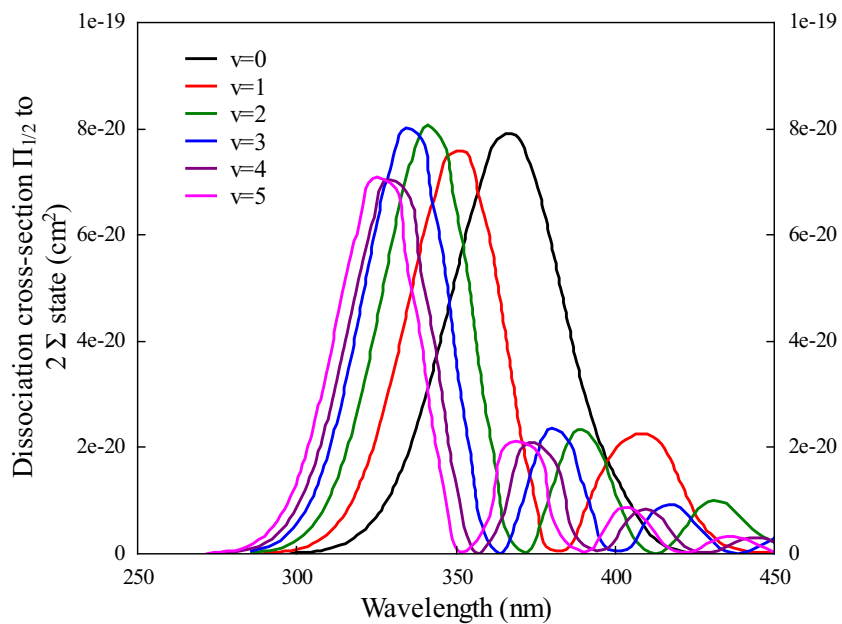
Figure 4.8. 1′-photon photodissociation crossection of IF$^+$ from $\Pi_{1/2}$ to 2Σ state from different vibrational levels ($v = 0 = 0,1,2,3,4,5$).
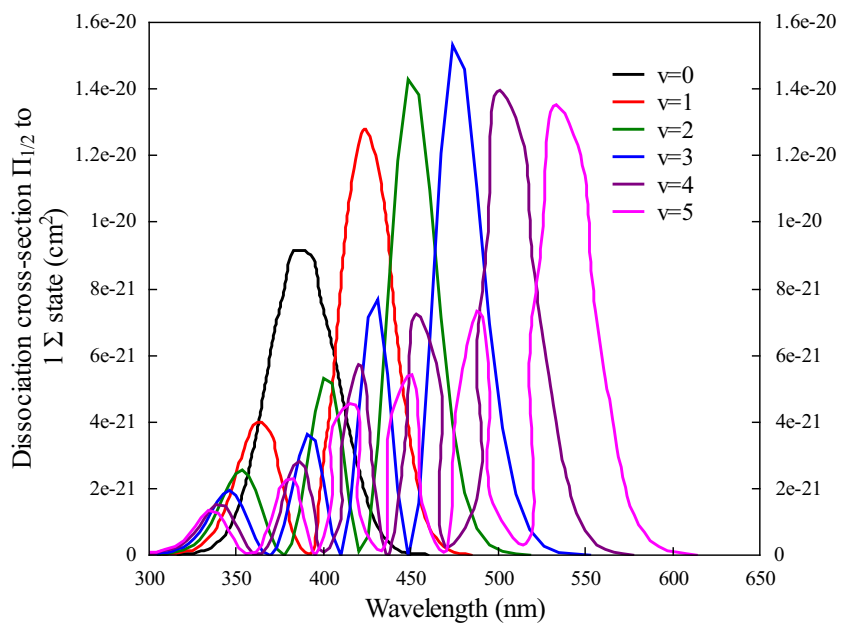
Figure 4.9. 1′-photon photodissociation crossection of IF$^+$ from $\Pi_{1/2}$ to 1Σ state from different vibrational levels ($v = 0 = 0,1,2,3,4,5$).

ranging from 1.06μm to 1.84μm and 1'-photon wavelengths as shown in Figs. 4.8, 4.9. These wavelengths look favorable making IF$^+$ a strong candidate for cooling.

ICl$^+$ and HI$^+$

Unlike IF$^+$, we do not have all the transition dipole moments for all relevant transitions in ICl$^+$ and HI$^+$ to determine the detailed 1-1' REMPD scheme [56], [57]. HI$^+$, like all hydrides, has the advantage of having most of the molecules in the $v = 0$ ground state as given in Table 4.2 giving us more molecules to work with when they are formed. Like IF$^+$, ICl$^+$ also has diagonal FCF as given in Table 4.3. Their potential as candidates can only be determined when these molecules are spectroscopically better understood.

4.4. Conclusion

In this chapter, potential candidates for recyclable spectroscopy and laser cooling have been discussed. For recyclable spectroscopy using molecules with laser-cooled atoms, BaF$^+$ and BaCl$^+$ look promising. BaH$^+$ could become be a possible candidate if the actual transition dipole moment function results in a smaller dissociation cross-section at the Ba$^+$ laser cooling wavelength. Though rate equation simulation of cooling rates and/or laser intensity calculations for the laser-cooling candidate molecules have to be run, preliminary analysis indicates that IF$^+$ looks promising.

References

[1] W. T. Scott, *American Journal of Physics 27, 4189 (1959).*

[2] B. Wang, J. W. Zhang, C. Gao and L. J. Wang, *Optics Express 19, 16438 (2011).*

[3] G. Leschhorn, T. Hasegawa and T. Schaetz, *Applied Physics B 108, 159-165 (2012).*

[4] A.V. Steele, L. R. Churchill, P. F. Griffin and M. S. Chapman, *Physical Review A 75, 053404 (2007).*

[5] P. Grundevik, M. Gustavsson, G. Olsson and T. Olsson, *Zeitschrift Fur Physik A-Hadrons and Nuclei 312, 1 (1983).*

[6] D. R. Denison, *Journal of Vacuum Science and Technology 8, 266 (1971).*

[7] P. K. Ghosh, Ion Traps, *Clarendon Press Oxford (1995).*

[8] L. D. Landau and E. M. Lifshitz, Mechanics, 3rd ed., Chapter 30: Motion in a rapidly oscillating field, *Pergamon Press Ltd. (1976).*

[9] P. L. Kapitza, Collected Papers of P. L. Kapitza, Volume II, 1938-1964, Chapter 45, *Pergamon Press Ltd (1965).*

[10] K. Mølhave, Construction of and Experiments with a Linear Paul Trap, *Master's thesis, Institute of Physics and Astronomy, Aarhus University (2000).*

[11] D. A. Dahl. SIMION 3D Ver 6.0 Users Manual, *Idaho National Engineering Laboratory, Chemical Materials & Processes Department, Lockheed Idaho Technologies Company, Idaho Falls (1995).*

[12] N. W. McLachlan, *Theory and application of Mathieu function, Oxford University Press (1947).*

[13] M. Drewsen and A. Brøner, *Physical Review A 62, 045401 (2000).*

[14] J. N. Tan, J. J. Bollinger, B. Jelenkovic and D. J. Wineland, *Physical Review Letters 75, 4198-4202 (1995).*

[15] J. P. Home, *Advances in Atomic, Molecular and Optical Physics 62, 231-277 (2013)*.

[16] F. H. J. Hall and S. Willitsch, *Physical Review Letters 109, 233202 (2012)*.

[17] K. Sheridan and M. Keller, *New Journal of Physics 13, 123002 (2011)*.

[18] N. Kimura, K. Okada, T. Takayanagi, M. Wada, S. Ohtani and H. A. Schuessler, *Physical Review A 83, 033422 (2011)*.

[19] R. Blatt and C. F. Roos, *Nature Physics 8, 277-284 (2012)*.

[20] M. Herrmann, V. Batteiger, S. Knünz, G. Saathoff, Th. Udem and T. W. Hänsch, *Physical Review Letters 102, 013006 (2009)*.

[21] T. Hasegawa, D. Tanooka and T. Shimizu, *Physical Review A 58, 2327 (1998)*.

[22] S. Knünz, M. Herrmann, V. Batteiger, G. Saathoff, T. W. Hansch and Th. Udem, *Physical Review A 85, 023427 (2012)*.

[23] B. G. Norton, E. W. Streed, M. J. Petrasiunas, A. Jechow and Q. D. Kielpinski, *New Journal of Physics 13, 113022 (2011)*.

[24] D. Offenberg, C. B. Zhang, Ch. Wellers, B. Roth and S. Schiller, *Physical Review A 78, 061401(R) (2008)*.

[25] G. E. Uhlenbeck and L. S. Ornstein, *Phys. Rev. 36, 823 (1930)*.

[26] R. Blatt, P. Zoller, G. Holzmüller and I. Siemers, *Zeitschrift fur Physik D-Atoms, Molecules and Clusters 4, 121-126 (1986)*.

[27] D. M. Meekhof, C. Monroe, B. E. King, W. M. Itano and D. J. Wineland, *Physical Review Letters 76, 1796 (1996)*.

[28] P. J. Shaw and D. J. Rawlins, *Journal of Microscopy 163(2), 151-165 (1991)*.

[29] D. F. V. James, *Applied Physics B 66, 181-190 (1998)*.

[30] M. Drewsen, A. Mortensen, R. Martinussen, P. Staanum and J. L. Sorensen, *Physics Review Letters 93, 243201 (2004)*.

[31] B. Roth, D. Offenberg, C. B. Zhang and S. Schiller, *Physical Review A 78, 042709 (2008)*.

[32] L. Ratschbacher, C. Zipkes, C. Sias and M. Kohl, *Nature Physics 8, 649-652 (2012)*.

[33] G. Leschhorn, S. Kahra and T. Schaetz, *Applied Physics B 108, 237-247 (2012)*.

[34] F. Brandi and F. Giammanco, *Optics Express 19, 25480 (2011)*.

[35] K. Abich, A. Keil, D. Reiss, Ch. Wunderlich, W. Neuhauser and P. E. Toschek, *Journal of Optics B 6, 18-23 (2004)*.

[36] J. Liang and P. C. Haljan, *Physical Review A 83, 063401 (2011)*.

[37] K. Sheridan and M. Keller, *New Journal of Physics 13, 123002 (2011)*.

[38] G. Morigo and H. Walther, *European Physics Journal D 13, 261-269 (2001)*.

[39] J. P. Home, *Advances in Atomic, Molecular and Optical Physics 62, 231 (2013)*.

[40] L. D. Carr, D. DeMille, R. V. Krems and J. Ye, *New Journal of Physics 11, 055049 (2009)*.

[41] A. C. Vutha, W. C. Campbell, Y. V. Gurevich, N. R. Hutzler, M. Parsons, D. Patterson, E. Petrik, B. Spaun, J. M. Doyle, G. Gabrielse and D. DeMille, *Journal of Physics B: Atomic Molecular Optical Physics 43, 074007 (2010)*.

[42] P. Jansen, L.-H. Xu, I. Kleiner, W. Ubachs and H. L. Bethlem, *Physical Review Letters 106, 100801 (2011)*.

[43] Ch. Daussy, T. Marrel, A. Amy-Klein, C. T. Nguyen, Ch. J. Bord and Ch. Chardonnet, *Physical Review Letters 83, 1554 (1999)*.

[44] X. Tong, A. H. Winney and S. Willitsch, *Physical Review Letters 105, 143001 (2010)*.

[45] I. Sivarajah, D. S. Goodman, J. E. Wells, F. A. Narducci and W. W. Smith, *Physical Review A 86, 063419 (2013)*.

[46] W. G. Rellergert, S. T. Sullivan, S. J. Schowalter, S. Kotochigova, K. Chen and E. R. Hudson, *Nature 495, 490-494 (2013)*.

[47] T. Schneider, B. Roth, H. Duncker, I. Ernsting and S. Schiller, *Nature Physics 6, 275-278 (2010)*.

[48] P. F. Staanum, K. Hojbjerre, P. S. Skyt, A. K. Hansen and M. Drewsen, *Nature Physics 6, 271-274 (2010)*.

[49] C.-Y. Lien, C. M. Seck and B. C. Odom, *arXiv:1402.3918 (2014)*.

[50] R. J. LeRoy *Univeristy of Waterloo Chemical Physics Research Report CP-329R3 (1993)*.

[51] R. J. LeRoy *Univeristy of Waterloo Chemical Physics Research Report CP-555R (1993).*

[52] D. V. Heijnsbergen, T. D. Jaeger, G. von Helden, G. Meijer and M. A. Duncan, *Chemical Physics Letters 364, 345 (2002).*

[53] A. R. Allouche, F. Spiegelmann and M. Aubert-Frecon, *Chemical Physics Letters 204, 3 (1993).*

[54] M.Ziòłkowski *unpublished.*

[55] F. Innocenti, M. Eypper, S. Beccaceci, A. Morris, S. Stranges, J. B. West, G. C. King and J. M. Dyke, *Journal of Physical Chemistry A 112, 6939 (2008).*

[56] A. Chanda, W. C. Ho, F. W. Dalby and I. Ozier *Journal of Chemical Physics 102, 22 (1995).*

[57] A. J. Yencha, M. C. A. Lopes and G. C. King, *Chemical Physics Letters 325, 559-567 (2000).*